

CONSTRAINED EVOLUTION OF A RADIALLY MAGNETIZED PROTOPLANETARY DISK: IMPLICATIONS FOR PLANETARY MIGRATION

MATTHEW RUSSO

Department of Physics, University of Toronto, 60 St. George St., Toronto, ON M5S 1A7, Canada.

CHRISTOPHER THOMPSON

Canadian Institute for Theoretical Astrophysics, 60 St. George St., Toronto, ON M5S 3H8, Canada.

Astrophysical Journal 2015, in press

ABSTRACT

We consider the inner \sim AU of a protoplanetary disk (PPD), at a stage where angular momentum transport is driven by the mixing of a radial magnetic field into the disk from a T-Tauri wind. Because the radial profile of the imposed magnetic field is well constrained, a deterministic calculation of the disk mass flow becomes possible. The vertical disk profiles obtained in Paper I imply a stronger magnetization in the inner disk, faster accretion, and a secular depletion of the disk material. Inward transport of solids allows the disk to maintain a broad optical absorption layer even when the grain abundance becomes too small to suppress its ionization. Thus a PPD may show a strong middle-to-near infrared spectral excess even while its mass profile departs radically from the minimum-mass solar nebula. The disk surface density is buffered at $\sim 30 \text{ g cm}^{-2}$: below this, X-rays trigger strong enough magnetorotational turbulence at the midplane to loft mm-cm sized particles high in the disk, followed by catastrophic fragmentation. A sharp density gradient bounds the inner depleted disk, and propagates outward to $\sim 1\text{--}2$ AU over a few Myr. Earth-mass planets migrate through the inner disk over a similar timescale, whereas the migration of Jupiters is limited by the supply of gas. Gas-mediated migration must stall outside 0.04 AU, where silicates are sublimated and the disk shifts to a much lower column. A transition disk emerges when the dust/gas ratio in the MRI-active layer falls below $X_d \sim 10^{-6}(a_d/\mu\text{m})$, where a_d is the grain size.

Subject headings: accretion, accretion disks — magnetic fields — planets and satellites: formation — protoplanetary disks — turbulence

1. INTRODUCTION

Our goal here is to develop a deterministic model for the re-distribution of mass in the inner part of a protoplanetary disk (PPD). When considering accretion through a thin disk, a central problem is the dependence of the specific torque (or the ‘viscosity’) on distance from the accreting star. This question remains unresolved in most contexts, but it is essential to understanding the presence of exoplanets in small orbits around sun-like stars.

The planets discovered by *Kepler* probe the development of the natal disk over a broad range of radius and time (Lissauer et al. 2014). Our focus here is on angular momentum transport driven by magnetic stresses internal to the disk, including both the laminar Maxwell stress $B_R B_\phi / 4\pi$, and the turbulent stress that is driven by the magnetorotational instability (MRI; Blaes & Balbus 1994; Gammie 1996).

When the active column is determined only by external ionization, these internal magnetic stresses do not support a steady mass flow through the disk. The sign of the change in the surface mass density Σ_g depends on the distribution of the seed magnetic field. Most MRI-based models assume a vertical seed field, whose radial distribution cannot yet be reliably calculated. This prevents a deterministic calculation of the disk evolution – a shortcoming which extends to torque models invoking magnetized winds (Pudritz & Norman 1986; Suzuki et al. 2010; Bai & Stone 2013).

It has long been realized that radial magnetic fields could have a strong influence on angular momentum transport in centrifugally supported flows, driven by the persistent winding of the magnetic field. A magnetocentrifugal wind from

the central star, interacting with the upper layers of the disk, is a natural source for such a seed radial field. Indeed, the kinetic pressure of a T-Tauri wind can dominate the pressure of any wind that might flow from the disk surface during the later stages of PPD evolution.

This seed magnetic field is relatively strong in the inner disk, as is the induced torque. As we demonstrate in this paper, this has the interesting consequence that MRI-driven mass transfer *removes* material from the inner disk. A detailed description of the vertical structure of such a radially magnetized disk, including non-ideal MHD effects, can be found in Russo & Thompson (2015; hereafter Paper I).

A PPD modeled with a uniform viscosity coefficient α has a gas surface density profile slightly flatter than the one obtained by radial smoothing in the solar system, $\Sigma_g \propto R^{-1}$ (e.g. D’Alessio et al. 1998; Menou & Goodman 2004). A similar profile is obtained by averaging over the Kepler planetary systems, but with a normalization an order of magnitude higher (Chiang & Laughlin 2013). Formation of these exoplanets in situ then poses a significant conundrum: either their assembly must be delayed long after the condensation of solids in the inner disk, or rapid migration must be suppressed (e.g. Ogi-hara et al. 2015).

A much different surface density profile $\Sigma_g(R)$ is obtained following an accretion outburst driven by runaway MRI activation of a heavy disk (e.g. Zhu et al. 2009): one finds $\Sigma_g(R)$ growing with radius up to a peak at $\sim 2\text{--}3$ AU, as limited by the onset of gravitational instability. (This is a plausible mechanism for FU Orionis-type outbursts, which may occur several times during the early formation of a PPD.) Evolving

this profile forward with the torque mechanism developed in Paper I, we find that the PPD does not regenerate an inner surface density cusp following its final accretion outburst.

The similarity between the mass profile deduced from the Kepler systems and a uniform- α disk may therefore be illusory. An alternative explanation can be found in terms of the stability of planetary architectures, with the mean separation between planets limited to a multiple of the planetary Hill radius (Chambers et al. 1996; Smith & Lissauer 2009; Funk et al. 2010).

Another longstanding puzzle involves the relatively brief interval over which PPDs appear as ‘transition disks’ with extended internal cavities in reprocessed stellar light (Strom et al. 1989; Williams & Cieza 2011). Here we show that the evolution toward a low- Σ_g profile can occur very rapidly, while the flux of dust into the inner disk remains high enough to maintain an optical absorption layer. The dust loading of material flowing inside ~ 1 AU can be determined from a competition between inward advection and adhesion and settling. Evolution to a transition disk does not then require a sudden or major structural change, merely a reduction in the dust loading of the accreting gas.

Although a secular depletion of gas in a PPD can clearly inhibit planetary migration, the presence of close-in exoplanets is also suggestive of a regulatory mechanism that maintains Σ_g high enough to permit some migration over a ~ 1 – 10 Myr timescale. As a first estimate, consider migration driven by linear Lindblad and corotation torques (‘linear Type I’: Goldreich & Tremaine 1980; Ward 1991). A planet of mass M_p and semi-major axis a moves radially on a timescale

$$t_I \equiv \frac{a}{da/dt} \sim \Omega^{-1} \left(\frac{c_g}{\Omega R} \right)^2 \frac{M_*^2}{\Sigma_g R^2 M_p} \\ \sim 1 \times 10^6 \left(\frac{\Sigma_g}{30 \text{ g cm}^{-2}} \right)^{-1} \left(\frac{M_p}{10 M_\oplus} \right)^{-1} \text{ yr}, \quad (1)$$

where M_* is the mass of the central star, Ω is the Keplerian angular frequency, and $c_g = (k_B T / \mu)^{1/2}$ is the isothermal sound speed in gas of mean molecular weight μ . Expression (1) points to a surface density $\Sigma_g \sim 30 \text{ g cm}^{-2}$ over ~ 0.03 – 1 AU. Although this torque model is greatly oversimplified, a migration timescale comparable to the above estimate is supported by more detailed considerations of planet migration in our model disk, as presented in the concluding section.

We identify the following feedback mechanism. A column $\sim 30 \text{ g cm}^{-2}$ is comparable to the column $\delta \Sigma_{g,\text{ion}}$ that can be ionized by stellar X-rays. Maintaining a moderate ionization level, which is essential to the MRI, also depends on a strong depletion in μm -sized dust grains. In a disk with Σ_g initially exceeding $2\delta \Sigma_{g,\text{ion}}$, most of the solid material settles close to the midplane, where the vertical component of gravity nearly vanishes.

As Σ_g is reduced by mass transfer through the outer MRI-active layers of the disk, the ionization level rises near the midplane, permitting the lofting of solid particles from the settled layer. This creates an abundance of small grains through catastrophic fragmentation, because collisions typically first occur high in the disk, where the particle drift speed greatly exceeds the fragmentation speed. Thus the penetration of X-rays to the midplane, accompanied by the excitation of MRI turbulence, leads to a strong feedback on the amplitude of the turbulence.

This mechanism for regulating Σ_g depends on the persis-

tence of a midplane particle layer over a period of Myrs. Small particles could well be depleted by planetesimal formation but, in the absence of large planets, are easily resupplied by inward drift from the outer disk, mediated by azimuthal gas drag.

1.1. Plan of the Paper

The model of a radially magnetized PPD developed in Paper I is reviewed in Section 2, and its radial structure is described in Section 3. The inflow of dust through the turbulent upper layer of a PPD, and the reprocessing of stellar light by this layer, is addressed in Section 7. The feedback of midplane particles on the disk viscosity results in a buffered sequence of MRI-active disk solutions, which are described in Section 5; a much lower gas column is obtained in the absence of dust.

The evolution of a global disk model is tackled in Section 6: a similar end result is obtained for different initial disk profiles. Characteristic timescales for planet migration are outlined in Section 8, along with broader implications of this disk model. The Appendix presents our calibration of a post-FU Ori outburst disk, at the stage where dust condenses out of the gas phase and MRI turbulence is truncated near the midplane.

Throughout this paper we will sometimes use a shorthand $X = X_n \times 10^n$, with quantity X in c.g.s. units.

2. REVIEW OF RADIALLY MAGNETIZED DISK MODEL

Vertical disk profiles are obtained (Paper I) by starting with a weakly magnetized PPD and a stellar wind, which forms a turbulent boundary layer with the upper disk. The radial magnetic field that is implanted into the boundary layer is gradually raised in strength to a maximum value ~ 1 G at 0.1 AU, corresponding to a split-monopole profile reaching $\sim 10^2$ G at the stellar radius $R_* \sim 2R_\odot$. The stellar wind sweeps back any poloidal magnetic field whose pressure is less than a fraction $\sim 10^{-2}(\alpha/0.1)$ of the disk thermal pressure; here α is the Shakura-Sunyaev viscosity coefficient.

The implanted radial field is quickly sheared in the toroidal direction, at a rate $-(3\Omega/2)B_R$, thereby triggering MRI activity. The growth of the toroidal field is eventually limited by transport into the deeper, weakly conducting layers of the disk. The magnetic pressure generated in the disk-wind boundary layer pushes the radial field downward, thereby exciting a toroidal field and MRI activity at progressively greater depths. This process terminates in a hydromagnetically ‘dead’ zone that extends to the midplane. Vertical transport of B_R and B_ϕ is mediated by (i) Ohmic drift; (ii) ambipolar drift; (iii) MHD turbulence that is generated by MRI; and (iv) turbulence driven by the wind shear in the boundary layer.

The T-Tauri wind is launched from the stellar magnetosphere and flows radially at $V_w \sim 400 \text{ km s}^{-1}$. It transfers mass at a rate $\dot{M}_w \sim 10^{-9} M_\odot \text{ yr}^{-1}$, which is consistent with $\sim 10\%$ of the accretion rate through our model disk. Such a ratio of outflow to inflow is motivated by observation (Calvet 1997) and by the spin rates of T-Tauri stars (Matt & Pudritz 2005).

The nominal upper boundary of the flared disk is defined by a balance between thermal pressure and the normal component of the wind ram pressure. The thickness of the disk material that is overturned by the wind, and into which the radial magnetic field is mixed, is limited by radiative cooling. We find $\delta \Sigma_g \sim 10^{-3} \text{ g cm}^{-2}$ in an upper layer of atomic H that is regulated to ~ 5000 K by electronic transitions. The deeper layers of the disk are mainly composed of molecular

TABLE 1
 MODEL PARAMETERS

Stellar Model Parameters	
M_*	M_\odot
R_*	$2 R_\odot$
R_X	$10 R_\odot$
L_*	L_\odot
L_X	$2 \times 10^{30} \text{ erg s}^{-1}$
T_X	1 keV
Wind Model Parameters	
\dot{M}_w	$10^{-9} M_\odot \text{ yr}^{-1}$
V_w	400 km s^{-1}
B_R^w	$1 (R/0.1 \text{ AU})^{-2} \text{ G}$
Turbulence Model Parameters	
$\tilde{\alpha}_{\text{MRI},0}$	0.1
$\alpha_{\text{mix},0}$	1
Am_{crit}	10
$\Lambda_{\text{O,crit}}$	100

H_2 , and cool to a temperature $\sim (1-5) \times 10^2 \text{ K}$ that is determined largely by the absorption of stellar optical light on dust grains (Chiang & Goldreich 1997). The accretion rate and disk optical depth are low enough that the midplane temperature and scaleheight are similar to those of a passively irradiated disk, $h_g = c_g/\Omega \approx 0.023 (R/\text{AU})^{9/7} \text{ AU}$. Both the atomic and molecular layers are therefore taken to be isothermal, with a smooth but rapid transition in temperature at the cooling column.

Ionization of the disk is dominated by thermal X-rays from the stellar corona. Particular care must be taken with respect to the dependence of ionization rate on radius. It is determined by an approximate solution to the radiative transfer equation that is consistent with the Monte Carlo results of Igea & Glassgold (1999), but drops off with radius more rapidly than the analytic fit used by Bai & Goodman (2009) (and employed in several recent numerical simulations). We take as fiducial values an X-ray luminosity $L_X = 2 \times 10^{30} \text{ erg s}^{-1}$ and an optically thin, thermal bremsstrahlung spectrum with temperature $k_B T_X = 1 \text{ keV}$. Refractory solids are assumed to be depleted from the gas, and the mass fraction of volatiles (C, N, O, Ne, and S) is reduced by a factor 10^{-2} compared with solar abundance. The abundance of free metal atoms with low ionization potential (e.g. Mg) is taken to be 10^{-3} of the solar abundance.

MRI activity is maintained at $\delta\Sigma_g$ ranging up to $10\text{--}30 \text{ g cm}^{-2}$, below which the instability is quenched by Ohmic and ambipolar drift. Here the radial transport of angular momentum may still be maintained by a laminar Maxwell stress $B_R B_\phi / 4\pi$ (Turner & Sano 2008; Okuzumi & Hirose 2011; Mohanty et al. 2013; Lesur et al. 2014). Depending on the magnetization, this ‘undead’ zone may extend to columns as high as $\delta\Sigma_g \approx 100 \text{ g cm}^{-2}$.

Our baseline disk profile is constructed by ignoring the adsorption of charged particles on the surfaces of μm -sized dust grains. This is consistent with a mass fraction X_d of grains of radius a_d smaller than $X_d/a_d \lesssim 10^{-4} \mu\text{m}^{-1}$ near the base of the MRI-active layer, and implies a net depletion below $\sim 10^{-2}$ of

the solar abundance.¹ In this paper, we investigate the effect of an enhanced dust abundance on the ionization and torque profiles.

The following two sections review further details of our calculation of the magnetic field profile in the disk, the rate of radial mass transfer, and the limitations imposed by non-ideal MHD effects on internal disk torques.

2.1. Non-ideal MHD Effects and Turbulence

We calculate the vertical profile of the background magnetic field (B_R, B_ϕ) and mass density ρ by combining the steady form of the induction equation

$$\frac{\partial \mathbf{B}}{\partial t} = \nabla \times (\mathbf{v} \times \mathbf{B}) - \frac{4\pi}{c} \nabla \times (\eta \mathbf{J} + \eta_a \mathbf{J}_\perp) = 0 \quad (2)$$

with the equation of magnetostatic equilibrium,

$$\frac{\partial}{\partial z} \left(\rho c_g^2 + \frac{B^2}{8\pi} \right) = -\rho \Omega^2 z. \quad (3)$$

Here $\mathbf{J} = c \nabla \times \mathbf{B} / 4\pi$ is the current density. In layers where the undular Newcomb-Parker mode is excited (Newcomb 1961), the density gradient is set to give marginal stability of this mode, $-d\rho/dz = \rho z / \gamma h_g^2$, with adiabatic index $\gamma = 7/5$. Then the scale height $h_g \sim c_g / \Omega$.

The Ohmic diffusivity (as derived from the diagonal component of the resistivity tensor) is rescaled to include the combined effects of MRI-driven turbulence and Kelvin-Helmholtz mixing near the boundary layer,

$$\eta = \eta_0 + \eta_{\text{MRI}} + \eta_{\text{mix}}; \quad \eta_0 \approx 235 (T/\text{K})^{1/2} x_e^{-1} \text{ cm}^2 \text{ s}^{-1}. \quad (4)$$

Hall drift and ambipolar drift are parameterized by (Wardle & Salmeron 2012):

$$\begin{aligned} \eta_H &\approx 2 \times 10^5 x_e^{-1} \left(\frac{B/G}{\rho_{-10}} \right) \text{ cm}^2 \text{ s}^{-1}; \\ \eta_a &\approx 7 \times 10^3 x_e^{-1} \left(\frac{B/G}{\rho_{-10}} \right)^2 \text{ cm}^2 \text{ s}^{-1}. \end{aligned} \quad (5)$$

Ohmic diffusion dominates in dense and weakly magnetized regions, while ambipolar drift is dominant in the opposite limit.

Hall drift turns out to play a significant role in sustaining a non-axisymmetric MRI in a strong toroidal magnetic field (Paper I), but is of secondary importance for vertical transport of the mean magnetic field. That is because the vertical component of the Hall-drift speed $v_{H,z} = -J_z / en_e$ is proportional to the radial gradient of B_ϕ . Even though $\eta_H > \eta_a$ throughout the MRI-active layer, vertical Hall drift is suppressed by an additional factor $\sim h_g / R$. This is true as long as the vertical field $B_z = O(h_g / R) B_R$.

The Ohmic and ambipolar Elsasser numbers

$$\Lambda_O \equiv \frac{v_A^2}{\eta_O \Omega}; \quad \text{Am} \equiv \frac{v_A^2}{\eta_a \Omega} \quad (6)$$

provide the most accurate local measure of the ability diffusion to limit the growth of MRI turbulence. Here $v_A = B / \sqrt{4\pi\rho}$ is the Alfvén speed. When either Elsasser number falls below a critical value, fields can diffuse across a perturbation before it can develop into turbulence.

¹ Throughout this paper, X and x are used to denote mass and number fraction, respectively.

We assume that the MRI is cut off at critical Elsasser numbers

$$\Lambda_{O,\text{crit}} = 100; \quad \text{Am}_{\text{crit}} = 10. \quad (7)$$

Our choice of $\Lambda_{O,\text{crit}}$ comes from three-dimensional shearing box studies, which typically invoke weaker starting fields (Sano & Stone 2002; Simon & Hawley 2009; Bai & Stone 2011; Flock et al. 2012). Different values of $\Lambda_{O,\text{crit}}$ and Am_{crit} change the magnitude of the radial mass flux through the disk by varying the active column, but have a weak effect on the radial dependence of the mass flux.

The choice of Am_{crit} is motivated in part by a linear, non-axisymmetric stability analysis of a toroidally magnetized disk that includes both Hall and ambipolar drift (Paper I). This stability analysis shows that the MRI is more easily sustained at high magnetization in the presence of a toroidal, as opposed to vertical seed field. The Poynting flux associated with a growing MRI mode is predominantly horizontal, in contrast with the case of a vertical seed field, where the Poynting flux is directed vertically. On this basis, vigorous MRI-driven turbulence is not suppressed in a background toroidal field by propagation out of the growth layer, as numerical experiments find it to be when the seed field is strong and vertical, $B_z^2/8\pi P \gtrsim 10^{-2}$ (Bai & Stone 2013).

A high toroidal magnetization is sustained in the upper disk, $B_\phi^2/8\pi P \sim 0.1\text{--}10$, and so we treat the MRI-generated stress as a perturbation to the background field pressure. The ambipolar diffusivity η_a is taken to depend only on the background field $B^2 = B_R^2 + B_\phi^2$. A first estimate of the equilibrium magnetization is obtained by balancing winding of the mean radial seed field B_R against vertical transport across a scale height c_g/Ω with a diffusivity

$$\eta_{\text{MRI}} = \alpha_{\text{MRI}} \frac{c_g^2}{\Omega} = \tilde{\alpha}_{\text{MRI}} \left(\frac{B_\phi^2}{8\pi P} \right)^\delta \frac{c_g^2}{\Omega} \quad (8)$$

where B_ϕ is the mean toroidal seed field generated by winding and $\tilde{\alpha}_{\text{MRI}}$ is constant. One finds (Paper I)

$$\frac{B_\phi^2}{8\pi P} = \left(\frac{3}{2\tilde{\alpha}_{\text{MRI}}} \right)^{2/(1+2\delta)} \left(\frac{B_R^2}{8\pi P} \right)^{1/(1+2\delta)}. \quad (9)$$

The main challenge here is to make an appropriate choice for the amplitude $\tilde{\alpha}_{\text{MRI}}$ and index δ . We find that $\text{Am} \sim 100\text{--}300$ up to a column $\delta\Sigma_g \sim 10\text{--}30 \text{ g cm}^{-2}$ below the surface, beyond which the free electron fraction x_e drops precipitously. (See Figure 1 in Paper I.) This is higher by a factor $\sim 10\text{--}30$ than in the simulations of Lesur et al. (2014), Bai (2014), and Gressel et al. (2015) which impose a vertical seed field, and in which MRI turbulence is only marginally excited. On the other hand, the magnetization is high enough that the scaling $\delta = 1/2$ which is found for weak seed fields in direct numerical simulations (Hawley et al. 1995) cannot be trusted. We choose ν_{MRI} to scale directly with the seed toroidal magnetic pressure, corresponding to $\delta = 1$:

$$\alpha_{\text{MRI}} \equiv \tilde{\alpha}_{\text{MRI},0} \frac{B_\phi^2}{8\pi\rho c_g^2} \left(\frac{\Lambda_O}{\Lambda_O + \Lambda_{O,\text{crit}}} \right) \left(\frac{\text{Am}}{\text{Am} + \text{Am}_{\text{crit}}} \right). \quad (10)$$

Here $\tilde{\alpha}_{\text{MRI},0} = 0.1$. The last two factors on the right-hand side of Equation (10) implement the cutoff of the MRI-generated stress at low values of Am and Λ_O .

The main results of this paper are not sensitive to this calibration of ν_{MRI} . The rate of mass transfer scales as $\sim \tilde{\alpha}_{\text{MRI}}^{1/3}$,

and one obtains inside-out mass depletion for δ in the full range $0.5\text{--}1$, as can be seen from Figure 2 of Paper I. We view our normalization as conservative, given that simulations of the MRI with a weak seed field demonstrate enormous growth of the Maxwell stress.

The active layer is defined by the column $\delta\Sigma_{\text{act}}$, measured below the top of the disk, where $\tilde{\alpha}_{\text{MRI}}$ is reduced by a factor 2 by Ohmic and ambipolar diffusion. Typically Λ_O reaches its threshold value higher in the disk than does Am , so that the quenching of the MRI is mainly driven by Ohmic losses.

The disk-wind boundary layer is strongly magnetized given the chosen wind parameters, but our enforcement of marginal Newcomb-Parker stability causes the scale height to saturate at $h_g \sim c_g/\Omega$. The turbulent diffusivity in the mixing layer is therefore taken to be

$$\eta_{\text{mix}} = \alpha_{\text{mix}} h_g (c_g^2 + v_A^2)^{1/2}. \quad (11)$$

We take $\alpha_{\text{mix}} = 1$ (with a sharp cutoff below the base of the boundary layer as given by Equation (48) of Paper I) representing the fact that the depth of the mixing layer is set by a balance between Kelvin-Helmholtz-driven overturns and radiative cooling. Given rapid mixing in the boundary layer, we adopt the upper boundary condition $B_\phi/B_R = -3/2$. The deeper profile of the disk, in particular its magnetization and turbulent amplitude, turn out to be insensitive to the value of η_{mix} and to the boundary condition on B_ϕ .

2.2. Angular Momentum Redistribution

Turbulence in a thin PPD redistributes the background magnetic field (B_R, B_ϕ) primarily in the vertical direction, but also transfers angular momentum in the radial direction. These two effects are respectively encapsulated in a renormalized magnetic diffusivity and viscosity. Here we simply equate these diffusivities, corresponding to unit magnetic Prandtl number:

$$\nu_{\text{MRI}} = \eta_{\text{MRI}}; \quad \nu_{\text{mix}} = \eta_{\text{mix}}. \quad (12)$$

This choice is supported by some numerical simulations of the MRI with an imposed vertical field (Fromang & Stone 2009; Guan & Gammie 2009; Lesur & Longaretti 2009).

The radial flow of disk material is driven by a combination of turbulent stresses and the laminar Maxwell stress. The time evolution of the disk can be calculated, following Lynden-Bell & Pringle (1974), from the equation of conservation of angular momentum for a ring of radial thickness δR and mass $\delta m = 2\pi R \Sigma_g \delta R$,

$$\frac{d}{dt} (\delta m \Omega R^2) = \delta m \cdot v_R \frac{\partial(\Omega R^2)}{\partial R} = \delta R \frac{\partial G}{\partial R}. \quad (13)$$

The total turbulent + laminar magnetic couple acting at radius R is

$$\begin{aligned} G(R) &= R \cdot 2\pi R \int dz \left(\rho \nu R \frac{\partial \Omega}{\partial R} + \frac{B_R B_\phi}{4\pi} \right) \\ &= -3\pi R^2 \Omega \langle \nu \rangle \Sigma_g + \frac{R^2}{2} \int dz B_R B_\phi \\ &= -3\pi R^2 \int dz (\alpha_{\text{MRI}} + \alpha_{\text{mix}} + \alpha_{\text{lam}}) P_g, \end{aligned} \quad (14)$$

where

$$\langle \nu \rangle = \Sigma_g^{-1} \int dz (\nu_{\text{MRI}} + \nu_{\text{mix}}) \rho. \quad (15)$$

and α_{MRI} , α_{mix} are the viscosity coefficients defined in Equations (8), (11). The parameter

$$\alpha_{\text{lam}} \equiv \frac{|B_R B_\phi|}{6\pi P_g} \quad (16)$$

exceeds α_{MRI} below the active region, and may also exceed α_{mix} in the disk-wind boundary layer where $B_\phi/B_R \lesssim 10$.

The local mass transfer rate

$$\dot{M}(R) = -2\pi R v_R \Sigma_g = \dot{M}_{\text{turb}} + \dot{M}_{\text{lam}}, \quad (17)$$

can be written in terms of local disk quantities when $\langle \nu \rangle \Sigma_g \propto R^{\gamma_\nu}$ and $\Omega^{-1} \int dz B_R B_\phi \propto R^{\gamma_B}$,

$$\begin{aligned} \dot{M}_{\text{turb}}(R) &= 3\pi(1+2\gamma_\nu)\langle \nu \rangle \Sigma_g; \\ \dot{M}_{\text{lam}}(R) &= \frac{1+2\gamma_B}{2\Omega} \int dz B_R B_\phi. \end{aligned} \quad (18)$$

The gas surface density evolves with time unless $\gamma_\nu = 0$, $\gamma_B = 0$:

$$\frac{\partial \Sigma_g}{\partial t} = \frac{1}{2\pi R} \frac{\partial \dot{M}}{\partial R}. \quad (19)$$

Linear winding of the radial magnetic field is sustained at lower values of x_e than is MRI turbulence. An upper limit on the Lorentz force is obtained by requiring the Ohmic contribution to the vertical electric field to be smaller than the contribution from the disk rotation,

$$\frac{4\pi\eta}{c^2} |J_z| < \frac{\Omega R}{c} |B_R|. \quad (20)$$

The torque density is given by

$$\frac{R}{c} J_z B_R = \frac{\partial}{\partial R} \left(R \frac{B_R B_\phi}{4\pi} \right), \quad (21)$$

so the laminar stress can be no larger than

$$-\frac{B_R B_\phi}{4\pi} \lesssim \frac{\Omega R^2}{\eta} \frac{B_R^2}{4\pi}. \quad (22)$$

Here $\eta \sim \max(\eta_O, \eta_a)$ as both Ohmic and ambipolar diffusion may be responsible for the reduced coupling of the magnetic field to the neutral particles. Here Ohmic diffusion dominates near the torque cutoff, corresponding to

$$\eta_O \gtrsim -\frac{B_R}{B_\phi} \Omega R^2, \quad (23)$$

or, equivalently,

$$x_e < 5 \times 10^{-17} \left| \frac{B_\phi}{B_R} \right| \left(\frac{T/100\text{K}}{R/\text{AU}} \right). \quad (24)$$

We find that $B_\phi/B_R \gtrsim 10^2$ is generated by linear winding in and below the active layer. The cutoff in laminar torque then sits at $\delta \Sigma_g \sim 10^2 \text{ g cm}^{-2}$ below the disk surface, and $x_e \sim 10^{-14}$.

3. RADIAL PROFILES

We now present radial profiles of the disk magnetization, turbulence, and rate of mass transfer. The radial magnetic field that is imposed at the surface of the disk is take to be

$$B_R(R) = \epsilon_B \times 10^{-2} \left(\frac{R}{\text{AU}} \right)^{-2} \text{ G}. \quad (25)$$

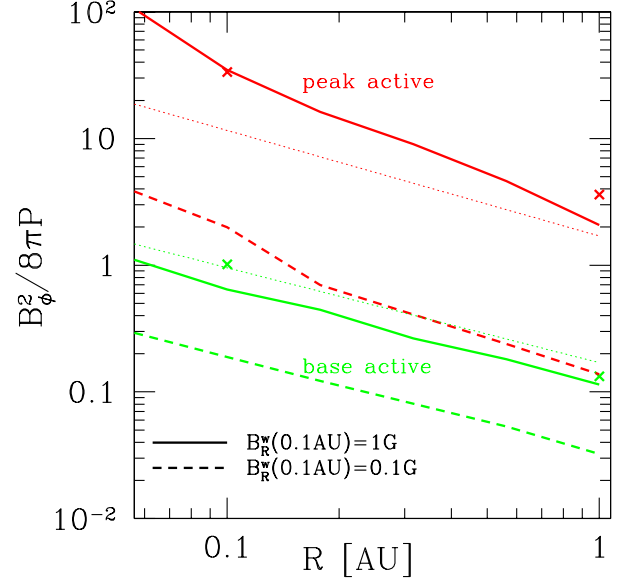


FIG. 1.— Maximum and minimum toroidal magnetization in the active layer of the disk. Curves refer to the more strongly magnetized hemisphere. The vertical magnetization profile has a sharp maximum outside ~ 0.1 AU from the protostar; the magnetization continues to drop below the plotted minimum below the base of the active layer. The analytic estimate (26) is drawn as red (green) dotted lines for $\delta \Sigma_g = 0.01$ (10 g cm^{-2}). The peak magnetization exceeds the analytic estimate at small radii, where it sits below 0.01 g cm^{-2} . ‘X’ marks the magnetizations that result from raising $k_B T_X$ to 5 keV from 1 keV.

Vertical disk profiles are obtained at cylindrical radii $R = 10^{-1.25} - 1$ AU (Paper I), and are now used to construct radial profiles of various disk properties. Section 6 treats the evolution of the disk.

We start with a total gas column $\Sigma_g = 200 \text{ g cm}^{-2}$, not much larger than the MRI-active column. Part of the motivation here is to check whether the disk evolves self-consistently to a low column. Given that the solids initially present in the inner disk have mainly settled to the midplane, the structure of the active layer would not be strongly modified by the presence of a thicker, quiescent layer below it. In addition, Σ_g grows with radius inside $\sim 2-3$ AU in the aftermath of an ionization-driven instability (Zhu et al. 2009; Appendix A). This means that the final evolution of the inner, layered disk may start with relatively little gas compared with uniform- α accretion models.

3.1. Equilibrium Magnetization

The upper disk becomes magnetically dominated in response to the embedding of a radial field of strength $\epsilon_B \sim 0.1-1$. The magnetization $B^2/8\pi P$ shows a pronounced peak at a relatively shallow depth within the active layer (Figure 1), which disappears inside ~ 0.1 AU. Below this peak, the magnetization drops monotonically toward the midplane, and in particular is lower at the base of the active layer where most of the radial mass transfer is concentrated.

The vertical profiles compare well with the analytic estimate (9). Substituting $P = \delta \Sigma_g c_g \Omega$ on the right-hand side of that equation and employing the temperature scaling $T =$

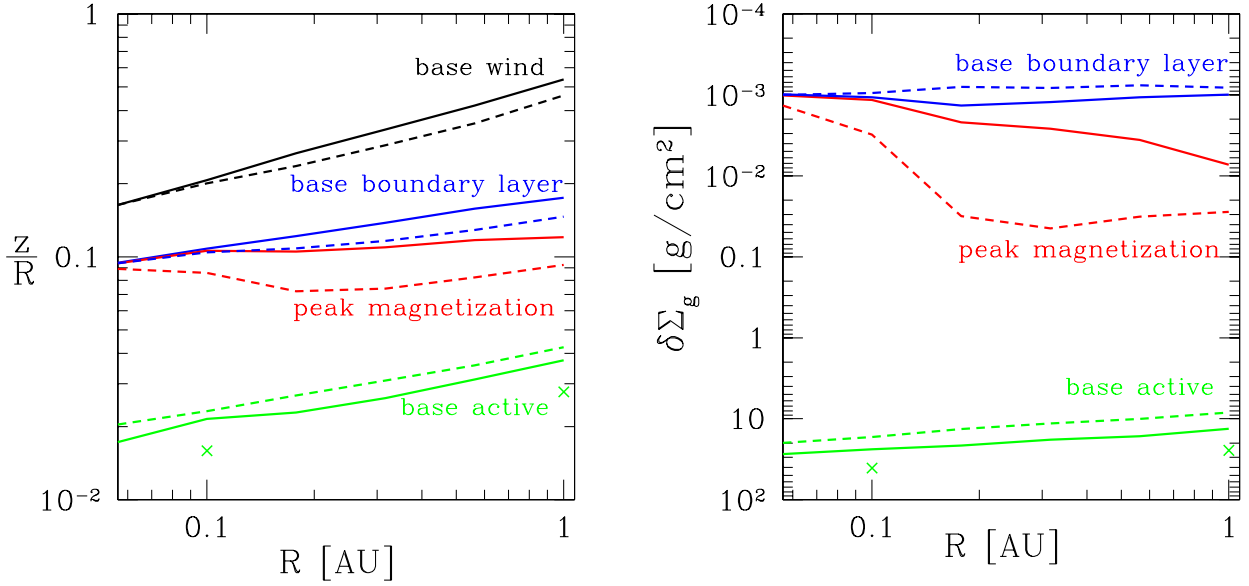


FIG. 2.— *Left panel*: heights of important reference points in the vertical disk profile, as a function of orbital radius. Solid lines: imposed magnetic field at full strength ($\epsilon_B = 1$); dashed lines: $\epsilon_B = 0.1$. *Right panel*: corresponding gas column as measured from the disk-wind interface. ‘X’ marks the base of the active layer when $k_B T_X$ is raised to 5 keV from 1 keV.

$180(R/\text{AU})^{-3/7}$ K, gives the equilibrium magnetization

$$\frac{B_\phi^2}{8\pi P} \approx 0.38 \left(\frac{\epsilon_B}{\tilde{\alpha}_{\text{MRI},-1}} \right)^{2/3} \left(\frac{R}{\text{AU}} \right)^{-0.76} \left(\frac{\delta \Sigma_g}{\text{g cm}^{-2}} \right)^{-1/3}. \quad (26)$$

This is also plotted in Figure 1 at the column $\delta \Sigma_g \sim 10^{-2}(R/\text{AU}) \text{ g cm}^{-2}$ of peak magnetization.

3.2. Vertical Structure

The disk is comprised of several layers, the transitions between which are shown in Figure 2. From the top: (i) the nominal boundary between hydrostatic disk and T-Tauri wind, where thermal pressure balances the normal component of the wind ram pressure; (ii) the base of the disk-wind boundary layer, where radiative cooling balances the input of turbulent kinetic energy from the damping of velocity shear; (iii) the surface of peak magnetization; and (iv) the base of the active layer, where $\Lambda_O \sim \Lambda_{O,\text{crit}}$. Our treatment of each of these transitions is discussed in more detail in Paper I.

The heights of these transitions all flare with radius. In spite of the high magnetization that is reached in the uppermost parts of the inner disk, this flaring is similar to that obtained in a thermally supported, Keplerian disk. This result is partly the result of our imposition of marginal stability to undular Newcomb-Parker modes: the zone of marginal stability expands to fill the active layer when the imposed magnetic field approaches the full strength considered, $B_R(0.1 \text{ AU}) \sim 1 \text{ G}$ ($\epsilon_B = 1$).

The column density $\delta \Sigma_{\text{act}}$ through the active layer is shown in the right panel of Figure 2. The analytic fit $\delta \Sigma_{\text{act}} \approx 13.4(R/\text{AU})^{-0.27} \text{ g cm}^{-2}$ applies at $\epsilon_B = 1$. The negative radial slope arises from the increased ionization rate in the inner disk, combined with the decrease of the toroidal field with radius, $B_\phi \propto R^{-1.33}$ near the midplane. By comparison, the base of the disk-wind boundary layer sits at a relatively uniform depth $\delta \Sigma_g \sim 10^{-3} \text{ g cm}^{-2}$.

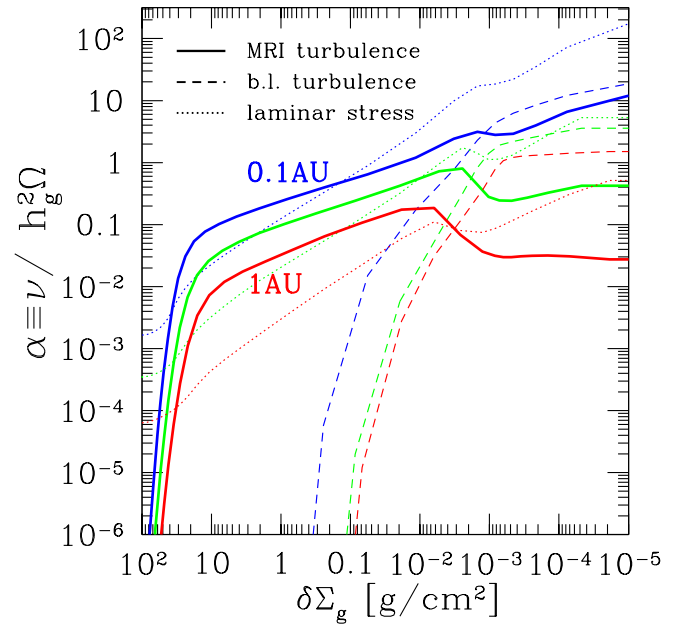


FIG. 3.— Solid lines: amplitude α_{MRI} of MRI-driven turbulence, Equation (10), as a function of column measured below disk surface. Dashed lines: amplitude α_{mix} of turbulence driven by disk-wind mixing (Equation (11) combined with Equation (48) of Paper I). Dotted lines: corresponding parameter (16) measuring the laminar stress $B_R B_\phi / 4\pi$. Blue, green and red lines show the profile at 0.1, 0.32 and 1 AU orbital radius.

An optical absorption layer is present in the disk as long as the mass fraction of $\sim \mu\text{m}$ sized solid grains exceeds $X_d \sim 10^{-6}$, as we show in Section 4. Its height varies from $\sim 2h_g = 2c_g/\Omega$ – within the lower part of the active layer – up to $\sim 6h_g$ as X_d is raised to solar abundance.

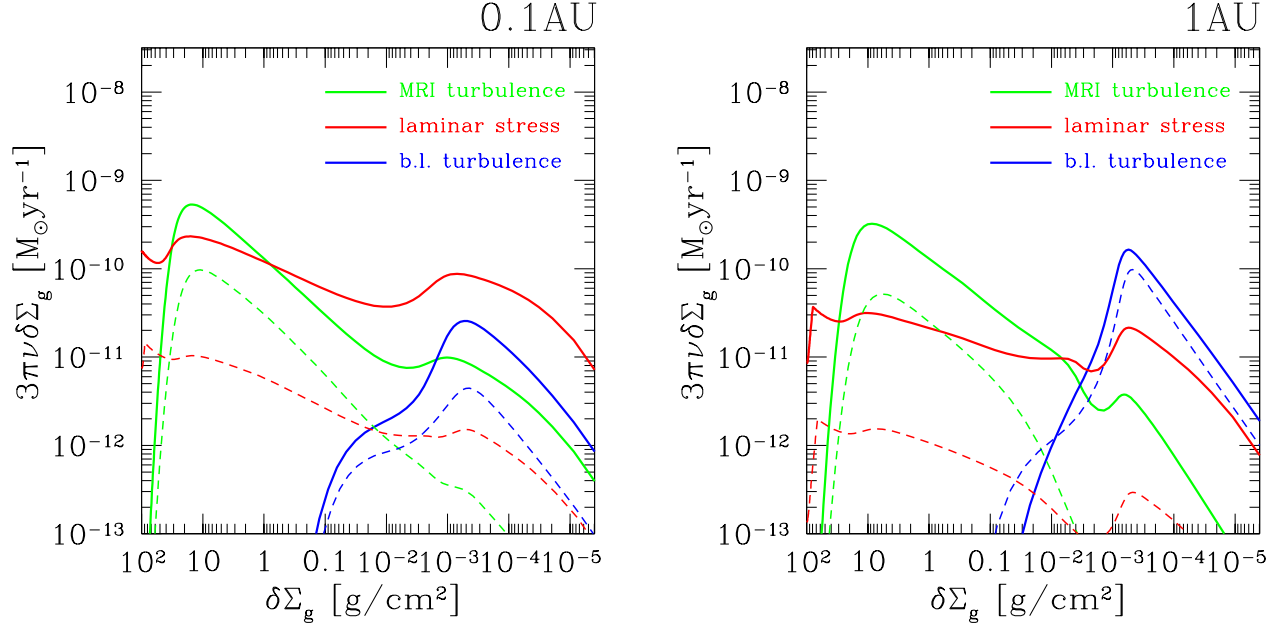


FIG. 4.— Differential contribution to radial mass transfer, versus column $\delta\Sigma_g$ below disk surface. The quantity $3\pi\nu\delta\Sigma_g$ is plotted separately for MRI, disk-wind turbulence, and laminar MHD stresses (green, blue, and red curves). For ease of comparison we define $\nu_{\text{lam}} = \alpha_{\text{lam}} c_g^2 / \Omega$ using Equation (16). When estimating accretion rates in this paper, we generally ignore the contribution from disk-wind turbulence. Solid and dashed lines correspond to $\epsilon_B = 1, 0.1$ where the imposed radial field is $B_R = \epsilon_B (R/0.1\text{AU})^{-2}$ G.

3.3. Mass Transfer Rate

Mass transfer in the disk is driven by a combination of MRI turbulence, the laminar stress $B_R B_\phi / 4\pi$, and turbulence in the disk-wind boundary layer. Figure 3 shows the vertical profile of the turbulent amplitudes α_{MRI} and α_{mix} . Turbulence driven by disk-wind mixing is cut off sharply below the boundary layer. The drop in α_{MRI} above $\delta\Sigma_g \sim 10\text{--}30 \text{ g cm}^{-2}$ reflects the onset of rapid Ohmic diffusion. The effective α parameter (16) representing the laminar torque is also shown.

The mass transfer rate that is contributed by these stresses is shown versus column depth $\delta\Sigma_g$ in Figure 4. Although α_{lam} only exceeds α_{MRI} in the diffuse upper disk and in the dead zone (where it is $\lesssim 10^{-5}$), the laminar stress still contributes significantly to \dot{M} closer than $\sim 0.1 \text{ AU}$ to the star.

Figure 5 shows the vertically summed contribution of each type of stress to the mass transfer rate. Each varies with distance from the protostar in a different way. Importantly, the two dominant contributions (driven by the MRI and by the laminar stress) both decrease with radius.

The MRI-generated flow depends on the strength of the linearly amplified (seed) toroidal field and the depth of the X-ray ionized layer. Combining Equations (8), (12), (18) and (26) gives

$$\begin{aligned} \dot{M}_{\text{MRI}}(R) &\approx 3\pi(1+2\gamma_\nu)\nu_{\text{MRI}} \cdot 2\delta\Sigma_{\text{act}} \\ &\approx 1.8 \times 10^{-8} \tilde{\alpha}_{\text{MRI},-1}^{1/3} \epsilon_B^{2/3} (1+2\gamma_\nu) \\ &\quad \times \left(\frac{2\delta\Sigma_{\text{act}}}{30 \text{ g cm}^{-2}} \right)^{2/3} \left(\frac{R}{\text{AU}} \right)^{0.31} M_\odot \text{ yr}^{-1}. \end{aligned} \quad (27)$$

One finds $\dot{M}_{\text{MRI}}(R) \propto R^{0.13}$ using the power-law fit to $\delta\Sigma_{\text{act}}(R)$. This is to be compared with the slightly negative gradient that is derived from the full vertical profiles (Figure 5). The difference arises from a somewhat larger α_{MRI} near the base of

the active layer in the inner disk.

We find that the laminar stress is competitive with the MRI stress at small radii, causing a non-negligible mass flux below the active layer. It also provides a strong contribution near the base of the boundary layer. One finds (Equation (8) of Paper I)

$$\begin{aligned} \frac{\dot{M}_{\text{lam}}}{\dot{M}_{\text{MRI}}} &\sim 2 \left(\frac{9\tilde{\alpha}_{\text{MRI}}}{4} \right)^{-2/3} \left(\frac{B_R^2}{8\pi P} \right)^{1/3} \\ &= 0.1 \left(\frac{\epsilon_B}{\tilde{\alpha}_{\text{MRI},-1}} \right)^{2/3} \left(\frac{\delta\Sigma_g}{30 \text{ g cm}^{-2}} \right)^{-1/3} \left(\frac{R}{\text{AU}} \right)^{-0.65}. \end{aligned} \quad (28)$$

Note that this expression does not include the additional contribution to \dot{M}_{lam} from the laminar zone below the MRI-active layer. In agreement with the numerical results, it shows a stronger decrease with radius than \dot{M}_{MRI} , and comes close to reproducing the amplitude plotted in Figure 4.

The sum $\dot{M}_{\text{MRI}} + \dot{M}_{\text{lam}}$ decreases with radius in both the numerical results and this analytic approximation (Figure 6). The analytic scalings $\dot{M}_{\text{MRI}} \propto \epsilon_B^{2/3}$ and $\dot{M}_{\text{lam}} \propto \epsilon_B^{4/3}$ are confirmed from the vertical profiles.

The mass flux driven by boundary layer turbulence increases with radius (recall that $h_g^2 \Omega \propto R^{3/2}$ for an atomic layer of uniform temperature 5000 K). It is negligible compared with \dot{M}_{MRI} , \dot{M}_{lam} when $\epsilon_B \sim 1$. Because the structure of the boundary layer is not yet calibrated by hydrodynamical simulation, we neglect its contribution to the disk evolution in Section 6.

The active column $\delta\Sigma_{\text{act}}$ is only logarithmically dependent on the inclination angle between disk surface and the stellar X-ray source. The height z_{act} of the ionized column is pushed to a larger number of thermal scale heights c_g/Ω .

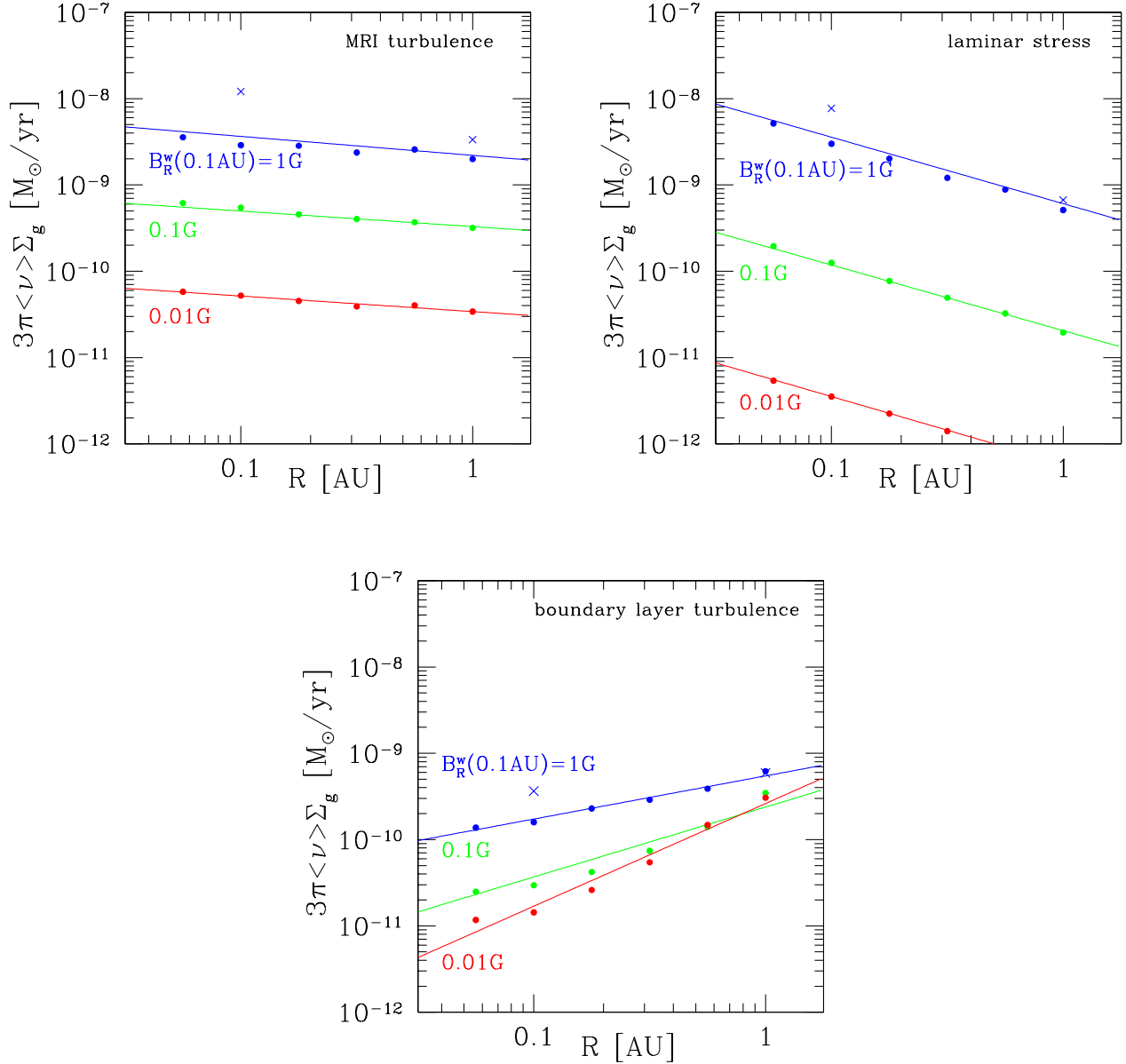


FIG. 5.— Mass transfer rate that is driven separately by turbulent, laminar and boundary layer stresses. The quantities plotted in Figure 4 are integrated over height in the more highly magnetized hemisphere, and doubled to represent a disk that is seeded by a reflection-symmetric wind magnetic field. Power-law fits (solid lines) for the strongest applied field ($B_R = 1$ G at 0.1 AU, $\epsilon_B = 0.1$) are, top to bottom, $2 \times 10^{-9}(R/\text{AU})^{-0.22}$, $6.1 \times 10^{-10}(R/\text{AU})^{-0.77}$, and $5.5 \times 10^{-10}(R/\text{AU})^{0.5} M_\odot \text{ yr}^{-1}$.

The pressure $P \sim \delta \Sigma_{\text{act}} g(z_{\text{act}}) = \delta \Sigma_{\text{act}} \Omega^2 z_{\text{act}}$ also increases. On the other hand, the scale height in the active layer decreases, $h_g \sim c_g^2 / g(z_{\text{act}})$. The net effect is to *decrease* the turbulent viscosity as deduced from Equations (8), (9), and (12):

$$\nu_{\text{MRI}} \propto \left(\frac{B_R^2}{8\pi P} \right)^{1/3} h_g c_g \propto z_{\text{act}}^{-4/3}. \quad (29)$$

This effect is only partly compensated by a mild increase in the equilibrium gas temperature resulting from the increased irradiation. We conclude that a negative scaling of $\dot{M}_{\text{MRI}} + \dot{M}_{\text{lam}}$ with radius is actually enhanced if the inner disk starts with a higher column than we are using to construct our vertical profiles (as it almost certainly does).

3.4. Inner Disk without Settled Particles

We now construct the surface density profile corresponding to steady accretion, $d\dot{M}/dr = 0$, through an inner disk without a significant mass of settled particles or embedded dust grains. Strong depletions of gas, to a surface density below $\delta \Sigma_{g,\text{ion}}$, are then obtained at accretion rates below $\sim 10^{-8} M_\odot \text{ yr}^{-1}$. If the disk is able to reach this state, then macroscopic (mm-cm sized) particles are self-consistently removed on a short timescale by inward drift. The case where the decrease of Σ_g is halted by a continuous supply of particles from the outer disk is explored in detail in Section 5.

The total gas column is obtained for a given \dot{M} by inverting $\dot{M} = \dot{M}_{\text{MRI}} + \dot{M}_{\text{lam}}$ using the profiles of ν_{MRI} and $B_R B_\phi / 4\pi$

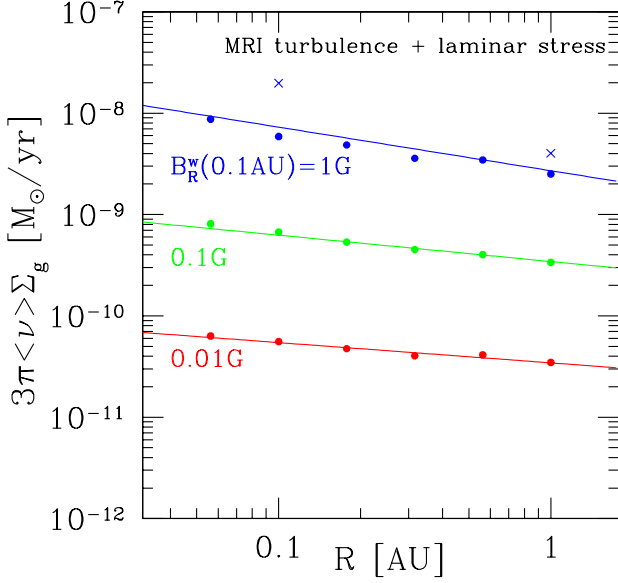


FIG. 6.— Net mass transfer rate through both hemispheres that is driven by turbulent and laminar stresses. Power-law fit for the strongest applied radial magnetic field: $3\pi\langle\nu\rangle\Sigma_{g,0} \approx 2.5 \times 10^{-9}(R/\text{AU})^{-0.4} M_\odot \text{yr}^{-1}$.

plotted in Figure 4. The result is shown in Figure 7.

One finds that the laminar torque dominates at small \dot{M} , resulting in very small total disk columns Σ_g . An accretion rate $\sim 10^{-9} M_\odot \text{yr}^{-1}$ can be supported by a total column of *atomic* gas as small as $\Sigma_g \sim 10^{-4} \text{g cm}^{-2}$ in the inner disk. This is primarily due to the highly efficient laminar stress in the boundary layer, where the mass transfer rate is

$$\dot{M}_{\text{lam}} = 8.5 \times 10^{-11} \left| \frac{B_\phi}{B_R} \right| \left(\frac{R}{0.1 \text{ AU}} \right)^{-1} T_{5000}^{1/2} \epsilon_B^2 M_\odot \text{yr}^{-1}. \quad (30)$$

This disk solution applies inside the sublimation radius R_{sub} of silicates (Equation (40)), even if settled particles are present further from the protostar. The resulting outward gradient in Σ_g has interesting implications for planetary migration (Section 8).

4. OPTICAL ABSORPTION LAYER IN A DUST-DEPLETED DISK

The disk profiles examined here assume that embedded dust has a minor impact on the ionization level sustained by stellar X-rays. This implies a mass fraction of μm -sized grains smaller than $X_d \sim 10^{-4}$. Such a level of dust depletion still allows the formation of an optical absorption layer. In other words, the disk can remain optically thick to stellar light even while the dust abundance is too small to reduce appreciably the equilibrium ambipolar Elsasser number Am . Here we show how the height of the optical absorption layer depends on the level of dust depletion.

The inner part of a PPD will not appear as a transition disk if its column is reduced to $\sim \delta\Sigma_{g,\text{ion}}$ and then sustained there by the fragmentation of settled particles. The brightness of the disk in the near-IR is more ambiguous if the column falls further to the low level shown in Figure 7.

Because the number density of dust grains is much smaller than that of free electrons, electron adsorption on grains is suppressed by the build-up of electric charge (see Ilgner &

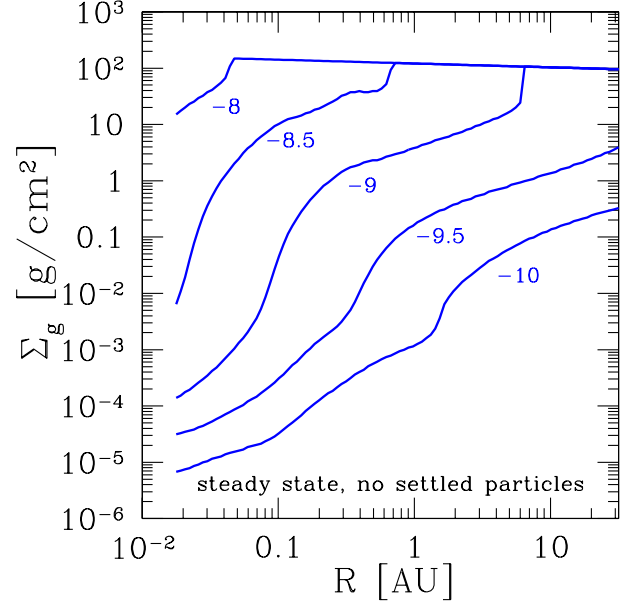


FIG. 7.— Steady state column density corresponding to accretion at a uniform rate in a dust-free disk. Curves obtained by integrating downward the vertical profiles of MRI and laminar stress. Labels correspond to $\log_{10}(\dot{M}_{\text{ss}}/M_\odot \text{yr}^{-1})$.

Nelson 2006; Bai & Goodman 2009, and Sections 3.3 and 3.4 of Paper I). Depletion of free electrons is then mediated by the adsorption of positively charged molecular ions and metal atoms, followed by recombination on grain surfaces. An estimate of the critical value of X_d is obtained by balancing the adsorption rate

$$\Gamma_{\text{ads}} = \pi a_d^2 n_d \left(\frac{8\mu_g}{\pi m_i} \right)^{1/2} c_g, \quad (31)$$

where a_d and n_d are the grain radius and number density, against the recombination rate $\alpha_{\text{eff}} n_e$ with a free electron in the gas phase. Our choice of recombination coefficient α_{eff} is given by Equation (23) in Paper I, corresponding to an abundance $x_M = 10^{-8}$ by number of free metal atoms. The geometric optical depth of spherical grains of mass density ρ_s through a disk of scale height h_g at a column $\delta\Sigma_{\text{act}}$ below its surface is

$$\tau_{\text{opt},r} \sim \frac{r}{h_g} \frac{3X_d \delta\Sigma_g}{4\rho_s a_d}. \quad (32)$$

Combining the above two equations with the relation between Am and x_e gives

$$\tau_{\text{opt},r} \lesssim 1 \times 10^2 \frac{(\text{Am}/10)}{(R/\text{AU})^{0.2} (T/200 \text{ K})^{0.4}} \left(\frac{\delta\Sigma_{\text{act}}}{10 \text{ g cm}^{-2}} \right)^{-0.2}. \quad (33)$$

The vertical models constructed in Paper I reach $\text{Am} \sim 100$ –300 in the active layer, and so allow a substantial optical depth.

At millimeter wavelengths, where the outer parts of PPDs are spatially resolved, depletion factors range from 0.1 to 10^{-3} compared with the interstellar dust/gas ratio $X_d \approx 10^{-2}$, and about 50% of PPDs in the Taurus region are depleted by more than a factor $\sim 10^{-3}$ in large grains (Furlan et al.

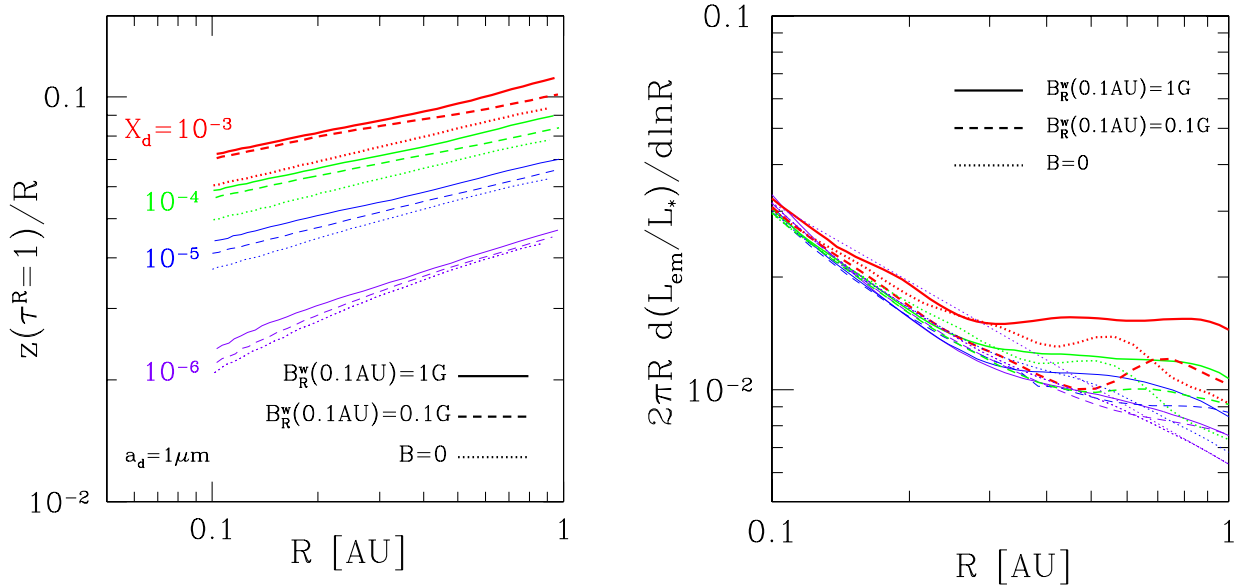


FIG. 8.— *Left panel*: height of the optical absorption layer, as a function of radius. Stellar photon source is taken to sit at $(R, z) = (0.9, 0.4)R_*$. Colors show different dust loadings of the MRI-active layer, as measured by X_d/a_d , where X_d is mass fraction of small grains of radius a_d . Disk ionization fraction is only weakly perturbed for $X_d/a_d \lesssim 1 \text{ cm}^{-1}$. Solid (dashed) curves: applied radial magnetic field $\epsilon_B = 1$ (0.1). Dotted curves: unmagnetized disk. *Right panel*: corresponding fraction of stellar luminosity that is re-radiated in various radial bins.

2006; D’Alessio et al. 2006). This depletion is frequently interpreted as evidence of grain growth and settling.

Previous modelling of the IR spectral energy distributions of T-Tauri and Herbig Ae stars is consistent with an optical absorption layer sitting 1–5 scale heights above the disk mid-plane (D’Alessio et al. 1999; Chiang et al. 2001). There is some evidence that the height of this layer decreases with age, reaching $z_{\text{opt}} \sim (2-3)h_g$ at a few Myr and before the formation of a transitional disk. The radial dependence of z_{opt}/h_g inside ~ 1 AU is only weakly constrained by mid-IR spectra, except in cases where a dust cavity is present (Williams & Cieza 2011).

We perform the exercise of varying X_d while fixing the disk mass profile. Here X_d is, for simplicity, assumed to be independent of radius. We focus on the radial distribution of the reprocessed IR emission from the flared disk surface. We only consider the reradiated fraction of the stellar luminosity L_* . The spectrum of the re-emitted IR also depends on the size distribution of grains, which is a complicated matter, and for that reason we do not attempt to model it here.

Our procedure is to calculate the optical depth along stellar rays over a range of polar angles, using a two-dimensional spline (in R, z) of the density profiles obtained in Paper I. The optical absorption layer is defined by the position on each ray where $\tau = 1$ in the visual band assuming $1 \mu\text{m}$ sized grains. Rays are taken to originate from a point $(R, z) = (0.9, 0.4)R_*$ on the star’s photosphere (determined by its average height), with $R_* = 2R_\odot$.

The height of the resulting absorption layer is shown in Figure 8 for $X_d/a_d = 10^{-1}, 1, 10 \text{ cm}^{-1}$. It increases from $\sim 2h_g$ to $\sim 5h_g$ as X_d/a_d is raised from 10^{-2} to 10. It should be kept in mind that fragmentation of grains in the upper disk will cause a_d to decrease inward, so that X_d/a_d need not be constant even for a uniform mass fraction of grains advected by accreting gas. The absorption layer begins to disappear from the inner disk when X_d/a_d drops below 10^{-2} cm^{-1} .

Figure 8 also shows that the fraction of L_* that is intercepted by each radial annulus of the disk varies weakly with the dust loading when $X_d/a_d \lesssim 1$, as is considered in this work. That is because the absorption layer flares more strongly outward for lower values of X_d/a_d , thereby compensating the smaller total angle z_{opt}/R that is subtended by the layer. In the upper range of X_d/a_d considered, the absorption layer maintains a simple profile, $z_{\text{opt}} \propto R^{9/7}$.

The stronger flaring of the absorption layer that is seen for smaller X_d/a_d is partly explained by the larger angle of incidence of the stellar photons reaching the inner disk: emission from a finite height above the disk tends to reduce the path length through the gas and push the absorption layer to a higher vertical gas column.

The absorption layer also expands vertically with increasing strength of the imposed radial magnetic field. In our disk model, this effect is strongly curtailed by imposition of (marginal) Newcomb-Parker stability. A mild flattening of the photosphere in the inner disk is caused by the slightly stronger magnetic support there. This also has the effect of introducing some mild shadowing of the disk at intermediate radii (~ 0.4 AU). The net effect is that the IR emission from our model disk is only weakly sensitive to the large radial variation in its internal magnetization.

5. RADIAL GAS FLOW LIMITED BY THE STIRRING OF SOLIDS

Our focus in this paper is on the flow of gas in a PPD after its self-gravity stops playing a significant role in angular momentum transport. Then solids condensed from the vapor phase will settle to the disk midplane over a broad range of radius (Chiang & Youdin 2010). Small grains rapidly stick to form larger particles at gas columns $\gtrsim \delta \Sigma_{g,\text{ion}}$, where MRI turbulence is strongly suppressed. Particles may grow to mm-cm sizes during settling (Goldreich & Ward 1973).

Here we consider the constraints on radial spreading that

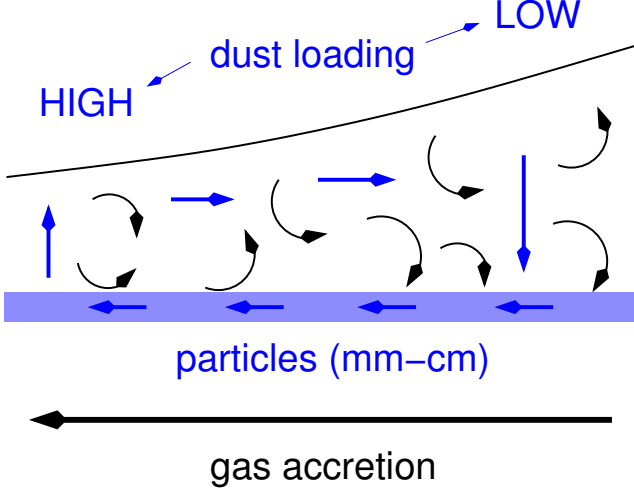


FIG. 9.— Cycling of macroscopic settled particles and lofted dust grains in a disk with gas column near the threshold for X-ray ionization of the midplane ($\Sigma_g \sim 10\text{--}30\text{ g cm}^{-2}$). The settled particles drift inward to supply a higher equilibrium dust abundance in the inner disk. The higher dust concentration there leads to outward diffusion of dust grains through the accreting gas. Re-adhesion of grains into larger particles allows excess dust to be removed from the outer disk.

are imposed by the continuing interaction of the gas with a settled particle layer. We are interested here in the behavior of the disk at a stage where Σ_g has *dropped* to the ionization threshold $2\delta\Sigma_{g,\text{ion}}$. We have been considering disks whose upper layers are depleted in dust. But even a relatively small surface density Σ_p in settled particles can suppress the MRI at $\delta\Sigma_g \sim 1\text{--}10\text{ g cm}^{-2}$ if the particles are lofted high in the disk, followed by catastrophic fragmentation. This corresponds to $\Sigma_p \gtrsim 10^{-4}(a_d/\mu\text{m})\delta\Sigma_{g,\text{ion}}$, where a_d is the size of the ‘dust’ fragments.

The settled particles orbit more slowly than the gas where the gas pressure decreases outward, and therefore drift inward toward the star. A surface density of settled particles at least comparable to the interstellar abundance $\sim 10^{-2}\delta\Sigma_{g,\text{ion}}$ can be sustained by inflow from the heaviest parts of the disk outside $\sim 1\text{ AU}$. We focus here on values of Σ_p below the critical value $(c_g/\Omega R)(\ell_p/h_g)\Sigma_g$ where vertical shear in the orbital velocity induces a strong Kelvin-Helmholtz instability in the particle layer Sekiya (1998). Here $\ell_p = P/|dP/dr|$ at the midplane. Then the mean density $\bar{\rho}_p$ of particles in the layer remains well below ρ_g , and the inward drift speed of particles (of stopping time t_{stop} and Stokes parameter $\text{St}_p = t_{\text{stop}}\Omega$) is $v_r = -\text{St}_p c_g^2/l_p\Omega$ (Goldreich & Ward 1973; Weidenschilling 1977).

The mass flow in particles that will sustain a given Σ_p is

$$\begin{aligned} \dot{M}_p &= -2\pi r v_r \Sigma_p = 2\pi \epsilon_{\text{dr}} \left(\frac{\Sigma_p}{\Sigma_g} \right) \frac{\rho_s a_p R c_g^2}{\Omega l_p} \\ &= 1.4 \times 10^{-12} \left(\frac{\Sigma_p/\Sigma_g}{10^{-3}} \right) \left(\frac{\epsilon_{\text{dr}} \rho_s a_p}{\text{g cm}^{-2}} \right) \left(\frac{R}{\text{AU}} \right)^{3/2} \\ &\quad \times \left(\frac{l_p}{r} \right)^{-1} \left(\frac{T}{200\text{K}} \right) M_\odot \text{ yr}^{-1}. \end{aligned} \quad (34)$$

The disk column is low enough that even macroscopic particles are in the Epstein drag regime; here $\epsilon_{\text{dr}} \sim 0.4$. The radial drift speed of the particles is high when $\Sigma_g \lesssim 2\delta\Sigma_{g,\text{ion}}$. It nonetheless remains below the fragmentation speed unless

the particles grow beyond $\sim\text{cm}$ radius.

We find that X_d is a strong decreasing function of radius in the MRI-active layer, when the dust abundance adjusts so as to sustain a steady inflow of *gas* through the inner disk. Then the inward drift of macroscopic particles is compensated by an *outward* diffusive flow of lofted dust grains, as depicted in Figure 9. The cycle can close within the disk when settled particles in the inner disk are lofted by turbulent gas eddies, and excess dust in the outer disk re-adheres into larger particles. We describe these processes in Section 5.2.

5.1. Equilibrium Surface Density Resulting from Particle Lofting and Midplane X-ray Ionization

The gas column that is maintained in the inner $\sim\text{AU}$ of an actively accreting PPD is the result of a competition between two effects: increased X-ray penetration to the midplane (which accelerates MRI-driven turbulence), and the lofting of solids from the midplane (which suppresses the turbulence). We note that the feedback of settled dust on the MRI has been considered by Jacquet & Balbus (2012), but without taking into account long-term secular changes in the gas column, or the effects of particle fragmentation.

At any depth in the disk, there is a critical dust loading above which the ionization level begins to be suppressed. Two effects are important here. First, an increase in the mass density of metals increases the X-ray opacity. This can reduce the ionization rate Γ_i by an order of magnitude at $\delta\Sigma_g \sim 10\text{ g cm}^{-2}$ when the dust abundance is restored to the solar value.

Second, as is reviewed in Section 4, the abundance of free electrons is suppressed by the charging up of grains, followed by the adsorption of positive metallic or molecular ions on grain surfaces (Equation (31)). In equilibrium we have $x_e \Gamma_{\text{ads}} = \Gamma_i$, which gives

$$x_e = \frac{4\rho_s a_d}{3\delta\Sigma_g \Omega} \left(\frac{\pi m_i}{8\mu_g} \right)^{1/2} \frac{\Gamma_i}{X_d}. \quad (35)$$

This expression holds when x_e is much smaller than $(\Gamma_i/\alpha_{\text{eff}} n_H)^{1/2}$; otherwise we revert to the expression corresponding to negligible adsorption.

Thus an enhancement in the dust abundance forces a reduction in the active column $\delta\Sigma_{\text{act}}$, which is defined by setting the cutoff factors in Equation (10) to 1/2. The result is shown in Figure 10. The reduction in $\delta\Sigma_{\text{act}}$ is driven mainly by enhanced Ohmic diffusion at low X_d , and by ambipolar drift at high X_d .

Below the layer of strong MRI activity lies a deeper and more weakly ionized zone, within which the turbulent motions are still fast enough to loft macroscopic particles from the midplane. We take for illustration a critical turbulent amplitude $\alpha_{\text{MRI}} \sim 10^{-4}$ for particle lofting. The corresponding stirring column $\delta\Sigma_{\text{stir},0}$ is plotted in the left panel of Figure 11 for a few values of the applied B_R . This column is obtained from our dust-free vertical disk profiles. For the maximum field strength considered ($\epsilon_B = 1$), we find $\delta\Sigma_{\text{stir},0} \approx 35(R/\text{AU})^{-0.2}\text{ g cm}^{-2}$. By way of comparison, the critical column for stirring is roughly three times larger than the total active column across the disk (Figure 2).

Adding a uniformly mixed population of small grains (we choose $a_d = 1\text{ }\mu\text{m}$) to the gas reduces the ionization level and both the active column $\delta\Sigma_{\text{act}}$ and the stirring column $\delta\Sigma_{\text{stir}}$. For each value of the grain mass fraction X_d , one can work out the adjusted ionization profile Γ_i and ionization level x_e from

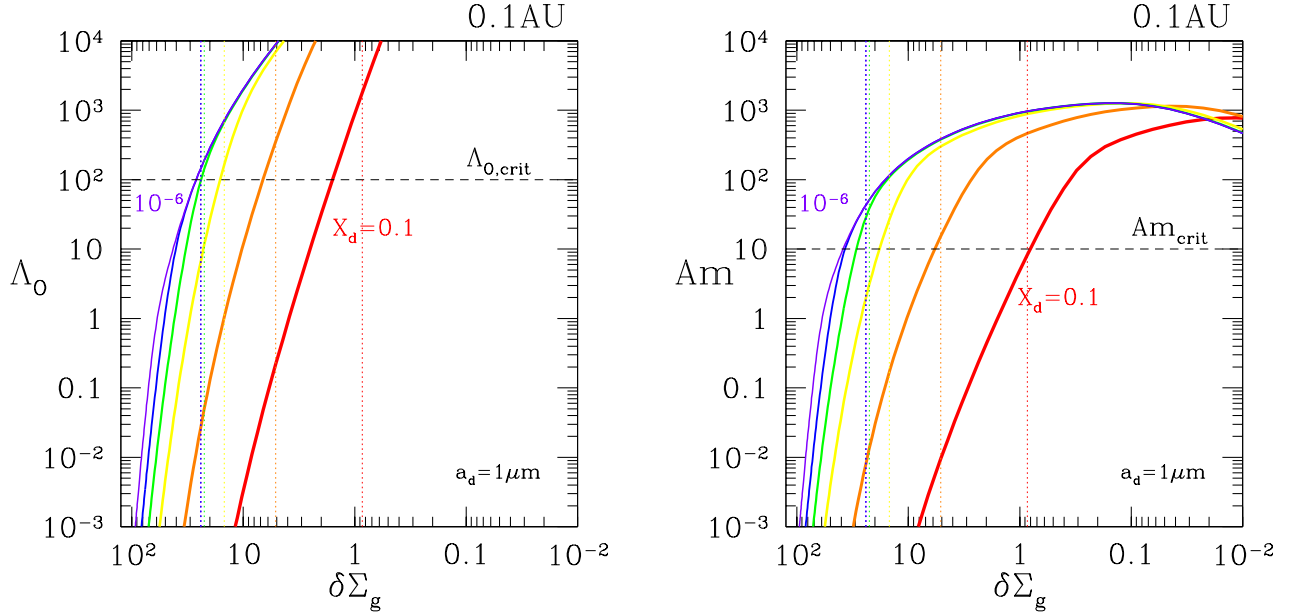


FIG. 10.— *Left panel:* Ohmic Elsasser number as a function of column $\delta\Sigma_g$ below the disk surface. *Right panel:* corresponding ambipolar Elsasser number. Dust with concentration parameter X_d/a_d is added to the vertical profile that was constructed in Paper I assuming $X_d = 0$. The ionization fraction is reduced according to Equation (35). Vertical dotted lines show the active column $\delta\Sigma_{\text{act}}$, at which non-ideal effects suppress α_{MRI} by a factor 1/2 according to Equation (10). The drop in $\delta\Sigma_{\text{act}}$ due to rising dust abundance is mainly caused by enhanced Ohmic diffusion at low X_d , and ambipolar drift at high X_d .

Equation (35) and calculate the resulting ambipolar number Am . (Note that the form of the ambipolar number given by Equations (5) and (6) is modified when grains are the main charge carriers, but this occurs at columns greater than $\delta\Sigma_{\text{act}}$ and so has very little effect for our purposes.) The adjustment in x_e is greater at larger $\delta\Sigma_g$, and disappears below the column where $X_{d,0} = X_d$. Here we take a short cut by maintaining the magnetic field profile $B_\phi(\delta\Sigma_g)$ of our zero-dust disk solutions, and then adjusting Λ_O through Equation (6). This in turn gives the re-scaled ambipolar number and MRI diffusivity ν_{MRI} using Equation (10).

The last step is to calculate a vertically summed accretion rate from the truncated profile of MRI activity at finite X_d ,

$$\dot{M}_{\text{MRI}} = 3\pi \langle \nu_{\text{MRI}} \rangle \cdot \delta\Sigma_{\text{stir}} = 3\pi \int_0^{\delta\Sigma_{\text{stir}}} \nu_{\text{MRI}} d\Sigma_g \quad (36)$$

and

$$\dot{M}_{\text{lam}} = \frac{1}{2\Omega} \int_0^{\delta\Sigma_{\text{stir}}} \frac{B_R B_\phi}{\rho_g} d\Sigma_g. \quad (37)$$

Figure 12 shows these quantities, together with the summed \dot{M} . We also obtain a vertically averaged viscosity coefficient $\langle \alpha \rangle = \dot{M} / 3\pi h_g^2 \Omega$, which is used in Section 8 to calculate the migration rates of planets within the disk.

In summary, we have obtained the mass transfer rate in a low-column disk where the ionization level is determined by a balance between (i) activation of the MRI near the midplane by X-ray ionization; and (ii) dust formation driven by the fragmentation of lofted particles. Analytic expressions for the separate contributions from turbulent and laminar Maxwell torques are

$$\dot{M}_{\text{MRI}} \approx 4 \times 10^{-9} \left(\frac{2\delta\Sigma_{\text{stir}}}{10^2 \text{ g cm}^{-2}} \right) \text{ M}_\odot \text{ yr}^{-1} \quad (38)$$

and

$$\dot{M}_{\text{lam}} \approx 5 \times 10^{-10} \left(\frac{2\delta\Sigma_{\text{stir}}}{10^2 \text{ g cm}^{-2}} \right)^{0.2} \left(\frac{R}{\text{AU}} \right)^{-0.7} \text{ M}_\odot \text{ yr}^{-1}. \quad (39)$$

The surface density profile $\delta\Sigma_g(R)$ corresponding to steady accretion through the inner part of a PPD can be obtained by inverting $\dot{M} = \dot{M}_{\text{MRI}}[\delta\Sigma_g] + \dot{M}_{\text{lam}}[\delta\Sigma_g(R)]$. The radial dependence of $\delta\Sigma_g$ is mainly determined by the radial variation of \dot{M}_{lam} .

Maintaining a steady mass flow in the inner disk requires the dust loading to increase to sharply towards the star, reaching $X_d \approx (0.1-1)(a_d/\mu\text{m})$ inside 0.1 AU. Although small grains are tightly bound to the gas, the strong negative dX_d/dr implies outward transport of grains within the MRI-active layer. Therefore a partly closed cycle of solids is possible in the inner disk, as sketched in Figure 9.

The residency time of the solids depends on their rate of leakage through the inner boundary of the dust-loaded disk. This boundary cannot push inside the dust sublimation radius,

$$R_{\text{sub}} = 0.04 \left(\frac{T_{\text{sub}}}{1800 \text{ K}} \right)^{-2} \left(\frac{L_\star}{L_\odot} \right)^{1/4} \text{ AU}. \quad (40)$$

Closer to the star, where the ionization level returns to the dust-free case, the surface density must drop sharply, to the level plotted in Figure 7. The inward transport of lofted grains could be suppressed outside R_{sub} by the strong outward force imparted by the absorption of stellar optical light. The transport of settled particles depends on how laminar the flow is near the inner boundary of the dust-loaded disk, an issue which is addressed in Section 7.

A higher loading of dust in the inner disk will raise the height of the optical absorption surface, thereby opening the possibility of disk self-shadowing. The absorption surfaces shown in Figure 8 are calculated for a uniform dust loading

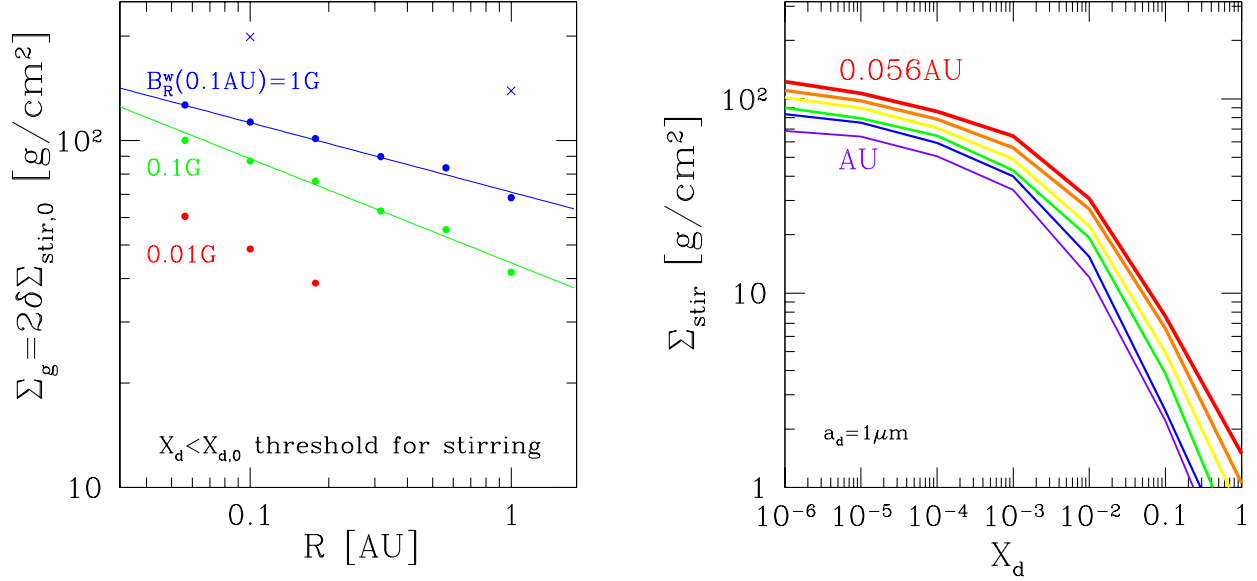


FIG. 11.— *Left panel*: threshold total gas column below which macroscopic (mm-cm sized) particles will be stirred up from the disk midplane, leading to catastrophic fragmentation and loading of the upper disk with small grains. Critical α_{MRI} for stirring is taken to be 10^{-4} , as described in the text. Colors correspond to different imposed radial magnetic fields. Power law fits are $\Sigma_g = 70 (R/\text{AU})^{-0.2}$ [$44 (R/\text{AU})^{-0.3}$] g cm^{-2} for $B_R = 1$ [0.1] G at 0.1 AU ($\epsilon_B = 1$, 0.1). *Right panel*: suppression of stirring column caused by rising dust abundance with uniformly mixed micron-sized grains. Colors correspond to different values of R , separated by 0.25 in $\log_{10} R$. Maintaining uniform \dot{M} in the inner disk requires progressively higher dust loadings toward smaller R .

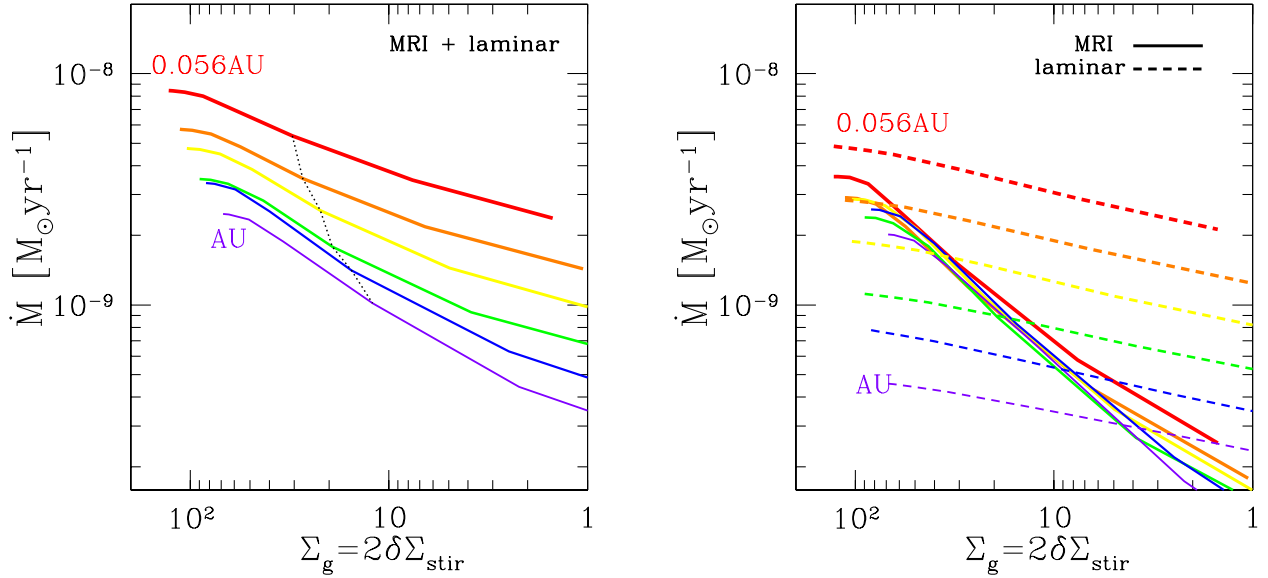


FIG. 12.— *Left panel*: total accretion rate in a disk whose active layer is limited in thickness by the lofting of particles and fragmentation into dust (Equations (36) and (37)). Points to the right correspond to higher dust mass fraction (up to $X_d = 1$ with micron-sized grains). Black dotted line: accretion rate $X_d \dot{M}$ of the lofted dust grains reaches a fraction 10^{-2} of the total accretion rate \dot{M} . Small grains must be sourced by inward-drifting particles in the midplane. When the corresponding solid particle accretion rate \dot{M}_p drops below $X_d \dot{M}$, the gas surface density is no longer buffered from below. Interior to this point, the disk transitions to much lower Σ_g as shown in Figure 7. *Right panel*: separate contributions to the accretion rate from MRI and laminar torques. The MRI contribution is directly related to $\delta\Sigma_{\text{stir}}$, hence the overlap of the solid curves.

X_d , and when $X_d/a_d \gtrsim 0.1 \text{ cm}^{-1}$ they coincide with nearly fixed multiples of the scale height. The finite size of the star reduces the shadowing effect of higher X_d in the inner disk. We find that the value of X_d that is implied by uniform accretion would produce enough absorption to block light from the stellar equator, but not from the poles. This partial self-shadowing would be further compensated by a modest reduction in gas scale height in response to the reduced irradiation of the inner disk. A self-consistent model of shadowing effects in a radially inhomogeneous and dust-loaded disk is beyond the scope of this paper.

5.2. Particle Lofting and Fragmentation, and Dust Settling

The accretion solutions obtained in Section 5.1 do not depend on the details of how macroscopic particles are lofted and fragment. Here we examine how an equilibrium concentration of small grains can be maintained by a competition between fragmentation and mutual grain sticking.

Even massive particles with $\text{St}_p > \alpha_{\text{MRI}}$ can be advected upward from the upper edge of the particle layer by individual eddies of speed $\alpha_{\text{MRI}}^{1/2} c_g$. When $\text{St}_p < \alpha_{\text{MRI}}^{1/2}$, this process only allows particles to reach a height $\sim c_g/\Omega$ above the midplane. But α_{MRI} increases rapidly upward to a value $> \text{St}_p$, meaning that some particles will continue to diffuse away from the midplane, into a thin column²

$$\Sigma_{g,\text{min}} \sim \frac{\epsilon_{\text{dr}} \rho_s a_p}{\alpha_{\text{MRI}}} \sim 10^{-1} \left(\frac{a_p}{\text{mm}} \right) \alpha_{\text{MRI},-1}^{-1} \text{ g cm}^{-2} \quad (41)$$

below the disk surface. Here the vertical diffusion speed of a particle of radius a_p drops below the vertical drift that is imposed by the disk gravity, $\alpha_{\text{MRI}} \sim \text{St}_p$.

A key point is that collisions between diffusing particles are delayed until their relative speed v_{col} rises well above the fragmentation speed ($v_{\text{frag}} \sim 1 \text{ m s}^{-1}$ for conglomerates of μm -sized silicate grains). That is because the vertical diffusion time $\sim \alpha_{\text{MRI}}^{-1} \Omega^{-1}$ is shorter than the mean time between collisions. The relative velocity of particles of somewhat different sizes is comparable to their drift speed through the gas,³

$$\begin{aligned} v_{\text{col}} &\sim (\alpha_{\text{MRI}} \text{St}_p)^{1/2} c_g \\ &\sim 20 \alpha_{\text{MRI},-1}^{1/2} \left(\frac{a_p}{\text{mm}} \right)^{1/2} (T/200 \text{ K})^{1/2} \\ &\quad (\delta \Sigma_g / 30 \text{ g cm}^{-2})^{1/2} \text{ m s}^{-1}. \end{aligned} \quad (42)$$

The net abundance of small grains results from a balance between destructive collisions involving a large particle with a high drift speed, and low-velocity collisions between grains which lead to coagulation. The production of small grains is dominated by a ‘sandblasting’ effect: a high speed collision between a large particle and a grain will eject a multiple Y of the grain mass (Jacquet & Thompson 2014). Then the mass density in grains $\bar{\rho}_d$ is determined by

$$Y \frac{\bar{\rho}_p}{m_s} \frac{\bar{\rho}_d}{m_d} \pi a_p^2 v_{\text{col}}(a_p) = \left(\frac{\bar{\rho}_d}{m_d} \right)^2 4 \pi a_d^2 v_{\text{col}}(a_d). \quad (43)$$

giving

$$\frac{\bar{\rho}_d}{\bar{\rho}_p} = \frac{Y}{4} \left(\frac{a_d}{a_p} \right)^{1/2}. \quad (44)$$

² The stopping time $t_{\text{stop}} \sim \epsilon_{\text{dr}} \rho_s a_p / \rho_g c_g$ when the particle size is smaller than the mean free path of H_2 molecules. Hence $\text{St}_p \sim \epsilon_{\text{dr}} \rho_s a_p / \delta \Sigma_g$.

³ Here the velocity field is assumed to have a Kolmogorov spectrum on a scale $< \alpha_{\text{MRI}}^{1/2} h_g$.

Experiments suggest $Y(v_{\text{col}}) \sim (v_{\text{col}}/v_{\text{frag}})^\beta$ with $1 < \beta < 2$ (Housen et al. 1983; Holsapple 1993).

This channel for dust production by stirred particles also allows for the removal of dust by the re-growth of particles, as we find is necessary to sustain a steady cycle of solids in the inner disk (Figure 9).

The upward flux of particles of mass m_s can be written as

$$\frac{dN_s}{dAdt} \sim \nu_{\text{MRI}} \rho_g \frac{\partial}{\partial z} \left(\frac{\bar{\rho}_p}{m_s \rho_g} \right). \quad (45)$$

Given that collisions are slow compared with vertical diffusion, the gradient of the particle concentration $\bar{\rho}_p/\rho_g$ is small. Then $\bar{\rho}_p \propto \rho_g$. The dust mass density varies with depth in the disk since it also depends on the particle drift speed through the yield Y (Equation (44)).

6. EVOLUTION OF THE INNER DISK

We now consider the clearing of mass from a PPD. This process is largely completed over the first $\sim 3\text{--}10 \text{ Myr}$ (Hernández et al. 2007), it appears by internal torques inside $1\text{--}2 \text{ AU}$, combined with a wind that is driven from the outer disk by the intense UV and X-ray flux from the protostar. A direct magnetorotational outflow from the disk surface is assumed to be suppressed by the pressure of the stellar wind, for the reasons outlined in Paper I. We also neglect turbulence that is driven by a purely hydrodynamical instability, e.g. vortices (Marcus et al. 2014).

We first prescribe the initial surface density profile. Three initial conditions are considered: the immediate aftermath of a FU Ori-like outburst following the recondensation of silicates; the ‘minimum-mass solar nebula’ (MMSN, e.g. Hayashi 1981); and a flatter density profile $\Sigma(R) \propto R^{-1}$ with the same normalization at 2 AU as the MMSN. The first profile is derived in Appendix A:

$$\begin{aligned} \Sigma_g(R) &= 3 \times 10^3 \left(\frac{R}{\text{AU}} \right) \text{ g cm}^{-2} \quad (R < R_Q \sim 2 \text{ AU}); \\ \Sigma_g(R) &= \frac{c_g \Omega}{\pi Q(R)} = \frac{c_g \Omega}{2\pi} \quad (R > R_Q). \end{aligned} \quad (46)$$

Here $Q = c_g \Omega / \pi \Sigma_g$ is the Toomre (1964) parameter for (axisymmetric) gravitational stability of a thin Keplerian disk. The inner zone is stable by this criterion ($Q > 2$), and the outer zone is marginally stable. In the second case,

$$\Sigma_{g,\text{MMSN}}(R) = 1700 \left(\frac{R}{\text{AU}} \right)^{-3/2} \text{ g cm}^{-2}. \quad (47)$$

The gas surface density is evolved according to

$$\frac{\partial \Sigma_g}{\partial t} = \frac{1}{2\pi R} \frac{\partial \dot{M}}{\partial R} + \left(\frac{\partial \Sigma_g}{\partial t} \right)_x, \quad (48)$$

where \dot{M} includes contributions from MRI and the laminar Maxwell stress. The last term on the right is the ionization-driven wind from Owen et al. (2012), specifically for a PPD with $\dot{M} \approx 1.3 \times 10^{-8} M_\odot \text{ yr}^{-1}$. In the parts of the disk with $\Sigma_g > 2\delta \Sigma_{g,\text{ion}}$, we use the power-law fit

$$\dot{M} \simeq 2.5 \times 10^{-9} (1 + 2\gamma) \left(\frac{R}{\text{AU}} \right)^\gamma M_\odot \text{ yr}^{-1} \quad (49)$$

from Figure 6. Here $\gamma = -0.4$ measures the gradient in the combined accretion rate $\dot{M} = \dot{M}_{\text{MRI}} + \dot{M}_{\text{lam}}$. This fit is used

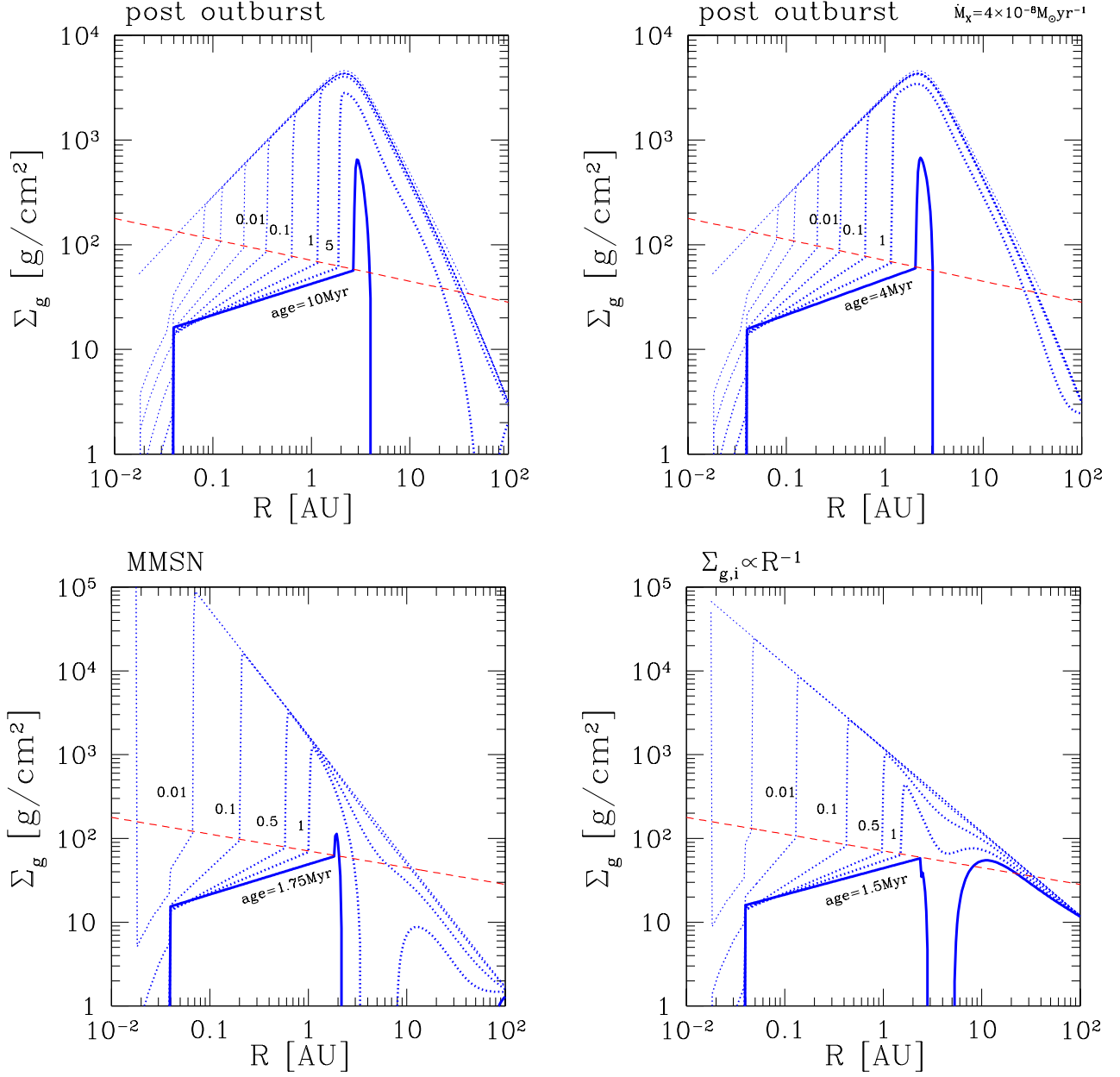


FIG. 13.— Long-term evolution of gas column, as driven by a combination of MRI and laminar MHD stresses, combined with the photoionization-driven mass loss rate of Owen et al. (2012). Buffering of the column at $\delta\Sigma_{\text{stir}} \approx 40(R/\text{AU})^{-0.2} \text{ g cm}^{-2}$ is due to the stirring up of solid particles and loading of the MRI-active layer by dust. *Top panels:* evolution following an FU Ori like outburst, starting from a time when silicates recondense in the disk and the ionization level near the midplane is suppressed by the formation of grains. Initial disk is marginally self gravitating ($Q = 2$) outside ~ 2 AU. Lifetime of the gas around ~ 1 AU varies inversely with the normalization of the X-ray and FUV driven mass loss rate ($\dot{M}_X = 1.3 \times 10^{-8}$ and $4 \times 10^{-8} M_\odot \text{ yr}^{-1}$ at left and right). *Bottom left panel:* evolution starting from the minimum-mass solar nebula; *Bottom right panel:* initial gas profile $\Sigma_g \propto R^{-1}$ with same normalization as MMSN at 2 AU.

beyond the maximum radius of 1 AU for which vertical disk profiles were constructed in Paper I, but close to this radius the ionization-driven wind begins to dominate.

Key outputs of the calculation include:

1. The surface density inside ~ 0.3 AU, where Kepler has discovered many planets. This decreases with time given the radial profile (49) of \dot{M} . This behavior is in sharp contrast with a uniform- α disk model, where $\langle \nu \rangle$ increases with radius due to the disk flaring and Σ_g increases with time from the initial state (46); see Zhu et al. (2009).

2. The outer radius R_{stir} of the ‘stirring’ region where the column has been reduced to $2\delta\Sigma_{\text{stir},0}$ (Figure 11) and the depletion of gas slows. This zone expands with time as gas is removed from the inner PPD. We recall from Section 4 that this depleted inner disk can maintain optical absorption surface, and at first will not appear as a transition disk.

3. The relative timing of the removal of the outer and inner disks, due to an ionization-driven wind and internal viscous stresses, respectively. We find that the outer disk is only modestly depleted after the inner disk reaches a surface density $\sim \delta\Sigma_{g,\text{ion}}$.

Because the accretion time is very short inside radius R_{stir} (compared with the time to excavate the intermediate parts of the disk), we take \dot{M} to be uniform in the inner, depleted disk. Then a significant drop in accretion rate is sustained at R_{stir} , and a sharp outward radial gradient in Σ_g forms there, associated with a local pressure maximum (Figure 13). We set the gradient scale of Σ_g to $4c_g/\Omega$ near the pressure maximum. No significant changes in the disk evolution are noticeable for order unity adjustments of this value.

The outward progression of the radius R_{stir} can be accurately estimated from

$$\frac{dR_{\text{stir}}^2}{dt} = \frac{\dot{M}_- - \dot{M}_+}{\pi \Sigma_g(R_{\text{stir}})} = \frac{1.27(R/\text{AU})^{-0.4}}{(\Sigma_g(R)/10^3 \text{ g cm}^{-2})} \frac{\text{AU}^2}{\text{Myr}}. \quad (50)$$

Here \dot{M}_- is the accretion rate everywhere inside radius R_{stir} , and is given by Equation (49) at R_{stir} with $\gamma = 0$. The accretion rate \dot{M}_+ just outside R_{stir} is smaller by a factor $1 + 2\gamma \simeq 0.2$.

The surface density profile interior to R_{stir} (and outside the sublimation radius (40)) is obtained as follows. The dust-loaded disk developed in Section 5 gives Σ_g as a function of the accretion rate \dot{M}_- through the inner disk. Expressing \dot{M}_- in terms of R_{stir} , we find the steady-state column to be

$$\Sigma_g = 2\delta \Sigma_{\text{stir},0}(R_{\text{stir}}) \left(\frac{R}{R_{\text{stir}}} \right)^{\gamma_s}; \quad \gamma_s = 0.5 \left(\frac{R_{\text{stir}}}{\text{AU}} \right)^{-0.5} \quad (51)$$

at $R_{\text{sub}} < R < R_{\text{stir}}$. The mild drop in Σ_g with time seen in the inner disk in Figure 13 is thus a result of the decreasing mass flux sourced by material near R_{stir} .

The dust loading X_d/a_d that is implied by Equation (51) varies strongly with radius. Figure 12 shows that the disk will sustain a given accretion rate at smaller R with a lower Σ_g , as a consequence of a higher dust loading. The accretion rate at R_{stir} is determined by the disk profile with vanishing dust loading. Moving inward toward the star, X_d/a_d rapidly increases.

The changing value of the index γ_s in Equation (51) also deserves comment. At early times, only a small inner part of the disk has a column reduced to $\sim \delta \Sigma_{\text{stir}}$. We find that the mass flux close to the star is mainly driven by the laminar torque (see Figure 12). Since the laminar Maxwell stress decreases strongly with radius, a variation in Σ_g is required to maintain a constant mass flux. As R_{stir} approaches 1 AU, MRI stresses begin to dominate. Since \dot{M}_{MRI} is nearly independent of radius at fixed $\delta \Sigma_{\text{stir}}$, the surface density profile flattens out. Additional flattening of $\Sigma_g(R)$ is caused by a weakening of the imposed radial field ($\epsilon_B \lesssim 0.1$ in Equation (25)), because the laminar stress scales more strongly with the applied field.

6.1. Details of Disk Evolution

Consider first the evolution of the disk from a post-FU Ori outburst configuration. Figure 13 shows that within ~ 1 Myr the inner disk is reduced to the stirring column out to ~ 1 AU. Over the same interval, the wind model of Owen et al. (2012) produces little clearing; this becomes significant only after ~ 5 Myr. Shortly after 9 Myr, a gap opens up outside 4 AU. The density bump inside it disappears in the next Myr, causing the inner disk to drain rapidly onto the star in ~ 0.1 My. The disk lifetime scales nearly inversely with the rate of mass loss due to photoevaporation, as is shown in the top right panel of Figure 13.

There is a slow decrease in the accretion rate onto the protostar as the dust-loaded inner disk expands (Figure 14):

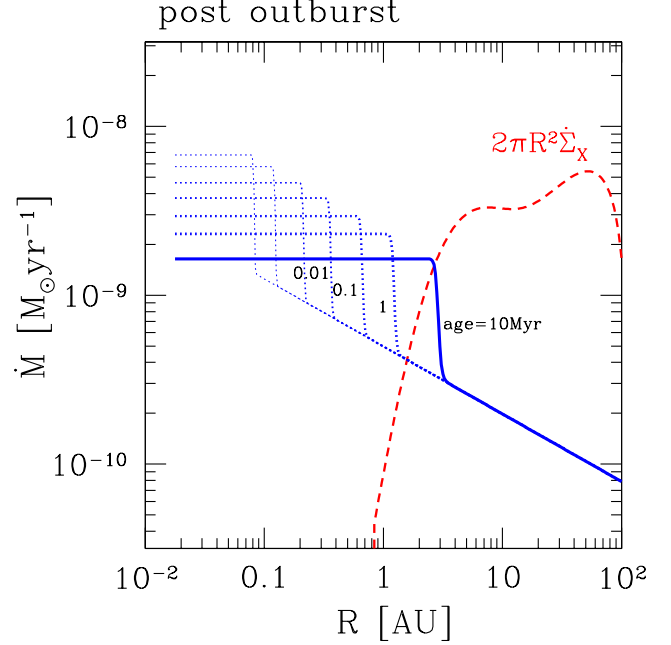


FIG. 14.— Blue lines: accretion rate versus radius and time corresponding to the top left panel of Figure 13. Red dashed line: mass loss rate in photoionization-driven wind according to the model of Owen et al. (2012).

from $\sim 10^{-8} M_{\odot} \text{ yr}^{-1}$ when R_{stir} sits at 0.06 AU, down to $2 \times 10^{-9} M_{\odot} \text{ yr}^{-1}$ as R_{stir} expands to 2 AU.

The dust-free solution with very low Σ_g is obtained inside $R_{\text{sub}} \sim 0.04$ AU, explaining the sharp upward rise in Σ_g at that radius in Figure 13. This inner pressure bump may expand outward, depending on the particle flux through the midplane region into the inner disk.

A lower total mass must be dispersed when starting the evolution with the MMSN model, because the Toomre parameter $Q \simeq 20$ is about 10 times larger than we choose in the ‘post-outburst’ disk model. (How the disk would reach such a state is not clear in the present context: angular momentum transport by spiral density waves would freeze out at lower Q , and so an additional source of torque would need to be invoked before the photoionized wind considered here would start.)

Clearing of the inner disk is initially a bit slower in this case, due to the inward-peaked surface density profile, but then picks up speed. Dispersal of the disk is completed within 2 Myr; this time is less sensitive to photoevaporative losses than in the post-outburst case since the density peaks at a smaller radius, where viscous evolution dominates photoevaporation.

The evolution of the flattest ($\Sigma_g \propto R^{-1}$) initial profile is distinguished from the other two by the persistence of gas at 10–100 AU after gas at ~ 1 –2 AU is largely removed. This is the same profile assumed in the models of Owen et al. (2012); not surprisingly, we also find that a distinct cavity develops around 2–3 AU. This case shows the greatest resemblance to transition disks, and the behavior of the ‘UV switch’ advanced by Clarke et al. (2001) to explain their relatively brief appearance.

7. GLOBAL TRANSPORT OF SOLID MATERIAL

Grains are supplied to the MRI-active layer of the inner disk through two channels: inward advection from a gas reservoir sitting outside ~ 1 AU; and a second, more indirect, channel involving the inward drift of macroscopic particles through

the disk midplane, followed by lofting and catastrophic fragmentation.

We first consider the residual dust mass fraction X_d when the turbulent motions at the disk midplane are too weak to loft particles. Then we consider the effect of a hydrodynamic instability, such as a baroclinic instability (Klahr & Bodenheimer 2003), which may be excited near the outward-propagating density peak. Here a narrow annulus of the disk will be directly exposed to a higher stellar radiation energy flux, and will develop a strong radial temperature gradient.

We must first develop a working criterion for the lofting of particles. This depends on establishing a connection between the turbulent amplitude and particle size. Here we employ a simple model of a ‘bouncing barrier’ (Zsom et al. 2010), representing the maximum size of compact solid particles that have been compressed to a low porosity by repeated mutual collisions. Surface van der Waals forces facilitate the sticking of $a_1 \sim \mu\text{m}$ -sized silicate monomers at relatively high collision speeds, up to $v_{\text{frag}} \sim 1 \text{ m s}^{-1}$. The critical speed for the sticking of larger, compact conglomerates (radius $a > a_1$) scales roughly as $v_{\text{stick}} \sim v_{\text{frag}}(a_1/a) \equiv k_{\text{stick}}/a$ (Chokshi et al. 1993).

Particles with Stokes parameter $\text{St}_p = t_{\text{stop}}\Omega \lesssim \alpha$ move through the gas, and with respect to each other, with a small velocity $v_{p-g} \sim (\alpha \text{St}_p)^{1/2} c_g \ll \text{m s}^{-1}$. Balancing this with v_{stick} at a column $\delta\Sigma_g \sim \rho_g c_g / \Omega$, one obtains

$$a \sim \left(\frac{k_{\text{stick}}^2 \delta\Sigma_g}{\alpha \epsilon_{\text{dr}} \rho_s c_g^2} \right)^{1/3}. \quad (52)$$

(Here stopping is self-consistently in the Epstein regime.)

At the threshold for setting, $\alpha \sim \epsilon_{\text{dr}} \rho_s a_p / \delta\Sigma_g$, and one finds

$$a_p \sim 0.01 \left(\frac{k_{\text{stick}}}{10^{-2} \text{ cm}^2 \text{ s}^{-1}} \right)^{1/2} \left(\frac{\delta\Sigma_g}{10^3 \text{ g cm}^{-2}} \right)^{1/2} \times \left(\frac{T}{200 \text{ K}} \right)^{-1/2} \text{ cm}. \quad (53)$$

The α parameter below which the particles settle corresponds to

$$\alpha < \alpha_{\text{set}} = 3 \times 10^{-5} \left(\frac{k_{\text{stick}}}{10^{-2} \text{ cm}^2 \text{ s}^{-1}} \right)^{1/2} \left(\frac{\delta\Sigma_g}{10^3 \text{ g cm}^{-2}} \right)^{-1/2} \times \left(\frac{T}{200 \text{ K}} \right)^{-1/2}. \quad (54)$$

7.1. Residual Grain Abundance in a Layered Disk

First consider a layered disk in which α attains a large value $\alpha_{\text{max}} \sim 10^{-2} - 10^{-1}$ at the top of the disk, and drops rapidly at columns $\delta\Sigma_g \gtrsim 10 \text{ g cm}^{-2}$. Then $\alpha_{\text{set}} \sim 3 \times 10^{-4}$ for silicate particles from Equation (54). Embedded particles diffuse vertically over a timescale $\sim \alpha^{-1} \Omega^{-1}$. Even in the relatively quiescent settling layer ($\alpha \sim \alpha_{\text{set}}$), this is faster than radial spreading through the turbulent upper disk, which occurs over the timescale $(r/h_g)^2 \alpha_{\text{max}}^{-1} \Omega^{-1} \sim 10^{3-4} \alpha_{\text{max}}^{-1} \Omega^{-1}$. Solid particles are therefore nearly uniformly mixed down to the depth at which mutual sticking allows them to settle out.

We are interested here in the residual density of small grains, which are easily suspended by MRI turbulence. The preceding considerations show that their depletion from the gas is limited not by mixing, but by the rate of mutual collisions, which is highest for the smallest particles. It is easy to

see that the largest contribution to the net collision rate (per unit area of disk) comes from the base of the layer where α begins to drop sharply (Figure 3). The collision rate between grains of mass $m_d \sim (4\pi/3)\rho_s a_d^3$ and space density $n_d = X_d \rho_g / m_d$ is

$$h_g \cdot n_d^2 4\pi a_d^2 v_{d-g} \sim X_d^2 \frac{\delta\Sigma_g \Omega}{(4\pi/3)\rho_s a_d^3} \left(\alpha_{\text{max}} \epsilon_{\text{dr}} \frac{\delta\Sigma_g}{\rho_s a_d} \right)^{1/2}. \quad (55)$$

Averaging vertically over the disk gives a characteristic collision time \bar{t}_{col} between small grains.

The formation of larger particles is suppressed if \bar{t}_{col} is longer than the time for radial inflow,

$$\bar{t}_{\text{col}} \sim \frac{1}{3X_d \Omega} \left(\alpha_{\text{max}} \epsilon_{\text{dr}} \frac{\delta\Sigma_{\text{act}}}{\rho_s a_d} \right)^{-1/2} \gtrsim \frac{1}{\alpha_{\text{max}} \Omega} \left(\frac{h_g}{R} \right)^{-2}, \quad (56)$$

corresponding to a dust loading

$$X_d \lesssim \frac{\sqrt{\alpha_{\text{max}} \text{St}_d}}{3\epsilon_{\text{dr}}} \left(\frac{h_g}{R} \right)^2 \approx 9 \times 10^{-7} \alpha_{\text{max},-1}^{1/2} \times \left(\frac{R}{\text{AU}} \right)^{4/7} \left(\frac{a_d}{\mu\text{m}} \right)^{1/2} \left(\frac{\delta\Sigma_{\text{act}}}{20 \text{ g cm}^{-2}} \right)^{-1/2}. \quad (57)$$

Larger particles easily form when this condition is violated.

The main conclusion here is that the dust population in the MRI-active parts of the inner disk is regulated by settling in the outer disk that feeds it. After the lapse of $\sim \text{Myr}$, a small fraction of the solids deposited initially at 1–2 AU will have swept through the inner disk, sustaining a population of μm or sub- μm sized grains.

7.2. Turbulent Transport Across Density Peak

Macroscopic particles near the outer edge of the depleted inner disk (radius R_{stir}) experience a combination of turbulent diffusion and secular drift toward the pressure maximum. In the absence of turbulence, the particles settle toward the midplane and the pressure maximum presents a barrier to their inward radial migration (e.g. Kretke & Lin 2007). A narrow density peak may, however, be susceptible to a hydrodynamic (e.g. baroclinic) instability. Without understanding details of such an instability, we can still formulate the following question: if the turbulence excited is strong enough to smear the density peak to a radial lengthscale $\Delta r \gtrsim h_g$, will it also transport particles across the peak?

Here it is essential to remember that the peak moves outward at a speed $dR_{\text{stir}}/dt \gtrsim 1 \text{ AU/Myr}$. Hence turbulence of amplitude $\nu_t = \alpha c_g^2 / \Omega$ will smear the peak over a scale given by $(\Delta r)^2 / \nu_t \sim (dR_{\text{stir}}/dt)^{-1} \Delta r$. The value of α corresponding to a given value of Δr is

$$\alpha \sim \frac{dR_{\text{stir}}/dt}{c_g} \frac{\Delta r}{h_g} \sim 3 \times 10^{-5} \left(\frac{dR_{\text{stir}}/dt}{1 \text{ AU/Myr}} \right) \left(\frac{\Delta r}{3h_g} \right). \quad (58)$$

Equation (54) indicates that this level of turbulence will suspend macroscopic particles at a gas column $\gtrsim 10^3 \text{ g cm}^{-2}$, which is comparable to the column that is attained by our post-FU Ori disk model at $R \sim 1 \text{ AU}$.

We conclude that a hydrodynamic instability that smears the density peak will also facilitate the inward flow of settled particles into the inner disk. Indeed, the dust loading of the inner disk may easily exceed the level (57) that is left behind in a layered disk with a quiescent midplane layer.

8. DISCUSSION

We have demonstrated that the inner $\sim 1\text{--}2$ AU of a PPD will quickly evolve to a mass profile very different from the one that is obtained by assuming a uniform viscosity coefficient α (or, indeed, as manifested in the popular MMSN disk model and its variant obtained from the *Kepler* planetary systems: Chiang & Laughlin 2013). Mass is removed from the inner disk as soon as a stellar wind flowing across its surface deposits a radial magnetic field into the upper layers of the disk. This radial field is wound up by the disk shear and then transported downward by a combination of turbulence and non-ideal MHD effects.

The vertical disk model so constructed in Paper I forms the basis for a constrained calculation of PPD evolution. The radial profile of the seed magnetic field is obtained directly from the profile of the imposed T-Tauri wind. We find that a depletion of mass from the inner disk is not sensitive to the details of how the MRI-generated stress depends on the seed (linearly wound) toroidal magnetic field. The rate of mass transfer through the disk depends only weakly on the normalization of this relation.

More standard MRI-based models (e.g. Gammie 1996; Zhu et al. 2009), which assume a vertical seed field, have the drawback that the flux distribution across the disk surface cannot yet be constrained in a useful way. The same limitation applies to models based on magnetorotational outflows from a vertically magnetized disk (Pudritz & Norman 1986; Suzuki et al. 2010; Bai & Stone 2013; Lesur et al. 2014; Gressel et al. 2015); these models also depend on an uncertain parameterization of the flux-to-mass ratio of the disk, and cannot yet be used to predict the sign of the change in mass in the inner part of a PPD.

Solid material in the inner disk is maintained by two sources: (i) small (μm sized) grains which are transported by MRI turbulence faster than they can stick together to form macroscopic particles; and (ii) macroscopic (mm-cm sized) particles which settle to the quiescent midplane and drift inward by the usual headwind effect (Goldreich & Ward 1973; Weidenschilling 1977).

We showed that suspended grains can have a small influence on the ionization level even while forming an optical absorption layer above a height $\sim 2h_g$. The radial distribution of reprocessed stellar light is found to depend weakly on the mass fraction X_d of dust grains in the MRI-active layer.

We also showed that the depletion of gas from the inner PPD is buffered by X-ray ionization of the midplane layer. Although this tends to activate the MRI, the lofting of macroscopic (mm-cm sized) particles from the disk midplane leads to catastrophic fragmentation higher in the disk, which loads the MRI-active layer with small grains. We found that steady accretion through the inner PPD can be sustained with a dust loading that varies with radius, but only over a finite range of \dot{M} . In this situation there is a strong inward gradient in X_d , meaning that suspended dust diffuses *outward* from the protostar. In this way, it may be possible to sustain a closed cycle of solids inside ~ 1 AU even while gas continues to accrete through the inner disk.

A conspicuous feature of our disk solution is a strong maximum in surface density which moves outward as the inner disk clears. This may create a visible excess of infrared radiation at a particular radius, although not as strong a spectral feature as would a rim bounding a transparent inner zone.

This maximum in Σ_g is also associated with a maximum in

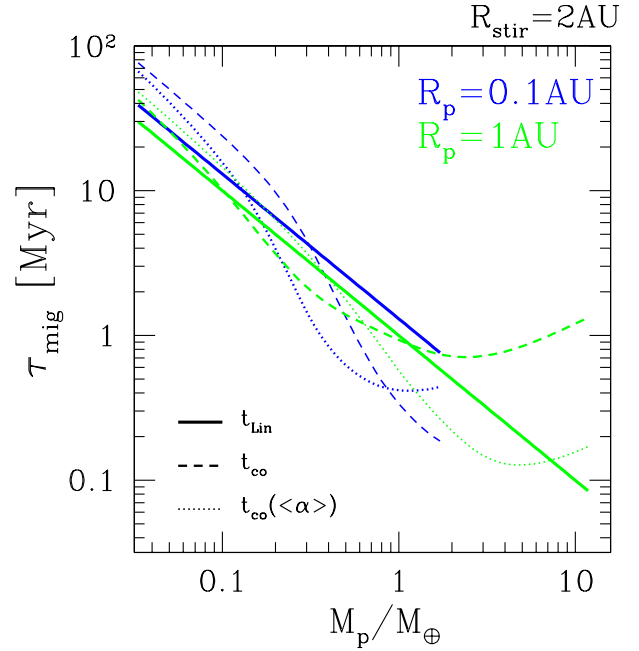


FIG. 15.— Migration time $|a/\dot{a}|$ of a planet of mass M_p in response to: linear Lindblad torques (negative torque, solid lines); or a combination of linear corotation torques and the non-linear horseshoe torque (positive torque, dashed and dotted lines), based on formulae tabulated in Paardekooper et al. (2011). In the second case, the transition from linear to non-linear torques and the saturation of the horseshoe torque is sensitive to the disk viscosity. Dashed curves assume α is normalized at the disk half-column; dotted curves make use of the vertically averaged viscosity $\langle\alpha\rangle$. Planet mass is constrained to lie below the ‘Hill’ mass given by $(M_p/3M_\star)^{1/3} = h_g/R$.

pressure, at which solid particles may collect. In contrast with the pressure bump associated with an ice sublimation surface (e.g. Kretke & Lin 2007), this feature scans through a wide range of radius. As such it is a possible site for the formation of planetesimals – although it should be kept in mind that settled particles will lag inside the pressure maximum as it moves outward. The gas near the bump is also susceptible to a hydrodynamic instability, especially a baroclinic instability, as a result of the strong radial temperature gradient that is generated by the raised disk profile (Klahr & Bodenheimer 2003). As a result, the particles still experience differential orbital motion with respect to the gas, along with vertical stirring.

8.1. Planets below the Gap Opening Mass

The equilibrium gas column of the dust-loaded inner disk is in a range that allows the inward migration of both Earth-mass and Jupiter-mass planets on a \sim Myr timescale. Figure 15 shows the migration time for planets smaller than the ‘Hill mass’, corresponding to $M_p = 3M_\star(c_g/\Omega R)^3$, based on the formulae of (Paardekooper et al. 2011) and the surface density profile shown in Figure 13. The solid lines in this figure are obtained from the sum of the inner and outer Lindblad torques, and represent inward migration (Goldreich & Tremaine 1980; Tanaka et al. 2002). The dashed and dotted lines show the summed effect of the linear and non-linear corotation torques, the latter imparted by gas executing horseshoe orbits in the corotation zone (Ward 1991). The corotation torque is positive, meaning that the net torque is negative (inward migration) where the dashed (or dotted) line lies *above* the solid line. Migration is outward where the opposite

inequality holds. For example, a M_\odot planet would experience very slow migration at 1 AU since positive and negative torques nearly cancel (with α normalized to the disk half column) but would migrate outwards at 0.1 AU due to a strong positive corotation torque.

The calculation includes the feedback of viscous and thermal diffusion on corotation torque saturation, again using formulae from Paardekooper et al. (2011). The disk viscosity has a strong vertical gradient (Figure 3), meaning that the upper disk can maintain an unsaturated corotation torque much more easily than the lower, quiescent disk. We evaluate the effect of the viscosity in two ways: first by adopting the value of the viscosity coefficient α at the half-column point in the disk (dashed lines); alternatively by using the vertically (mass) averaged $\langle\alpha\rangle$ (dotted lines). With the first prescription, planets of mass $\sim 1\text{--}10M_\oplus$ migrate inward at 1 AU, but migration stalls before the planet reaches 0.1 AU.

It should be emphasized that the magnitude of the corotation torque experienced by a planet below the gap-opening mass is sensitive to the dust loading of the gas in the co-orbital region. Repulsion of settled particles from the planet’s orbit (which requires a lower planet mass than does the repulsion of gas) would lead to a reduction in dust loading. Our flow solution with low X_d has a much lower gas column (Figure 7) than does the solution in which ν_{MRI} is regulated by the lofting of dust (Figure 11). Therefore the formulae of Paardekooper et al. (2011) may overestimate the horseshoe torque in a PPD with settled particles. Figure 15 provides a reasonable estimate of the magnitude of the orbital torque, but not necessarily of its sign.

8.2. Jupiter-mass Planets

The inward migration of Jupiter-mass planets through our model disk is buffered by the cumulative transport of mass, because the planet mass $M_p \gg \Sigma_g R^2$. This migration regime was first studied by Syer & Clarke (1995); we adopt a migration rate $\dot{a}/a \simeq -\dot{M}/M_p$ as reported by Duffell et al. (2014) in a numerical for a Jupiter-mass planet in a $\alpha = 10^{-2}$ PPD. The planet is started at the outer boundary R_{stir} of the dust-loaded inner disk and allowed to migrate inward without accreting. Figure 16 shows that over the final few Myr of disk dispersal, planets of mass $\sim 1\text{--}3M_J$ will migrate partly toward the protostar.

This result depends mainly on the accretion rate through the inner disk. Realistically, the planet will accrete part of the mass incident on its orbit (Lubow et al. 1999), but it is straightforward to show that this does not substantially change the result.

As the accretion rate drops, as it inevitably must as the outer parts of the PPD are removed, Σ_g must transition to the much lower steady-state value shown in Section 3.4, corresponding to a radially magnetized disk in which the dust abundance is everywhere too small to perturb the ionization fraction. This represents a second stage of inside-out partial clearing, during which the inner disk may become transparent to optical photons. Once this happens, gas-mediated planetary migration must freeze out.

A transition to a much lower gas column will also occur at the radius ~ 0.04 AU where solid silicate material that is directly irradiated by the disk will be sublimated. As a result, our disk model predicts the formation of a planet trap at this radius, where even the migration of a Jupiter-mass planet will be stalled. The existence of a ‘pile-up’ of hot Jupiters at this

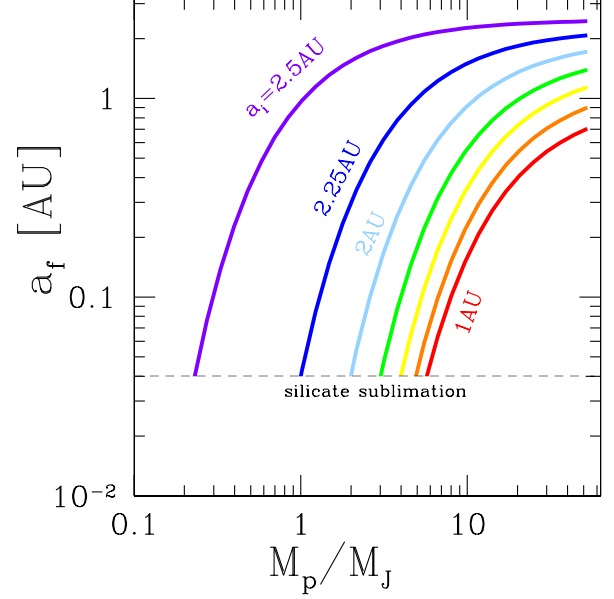


FIG. 16.— Final orbital semi-major axis a_f of a gap-opening planet, as a function of mass. Planet migrates inward according to the rate determined by (Duffell et al. 2014) at various times in the evolution of the disk shown in Figure 13. Planet is assumed not to accrete from the disk; partial accretion of the gas leads to a modest increase in a_f .

radius is presently controversial, depending on an evaluation of how the orbits are sampled observationally (Winn & Fabrycky 2015).

8.3. Transition Disks as a Probe of the Disk Mass Profile During Planet Formation

We have combined our mass transfer model for the disk inside $\sim 1\text{--}2$ AU with the photoionization-driven wind formulated by Owen et al. (2012). Considering a range of initial mass profiles (including a post-FU Ori outburst configuration, the MMSN profile, and a flatter $\Sigma_g \propto R^{-1}$ initial profile), we find that the clearing of gas from inside $1\text{--}2$ AU is insensitive to the initial profile. In most cases, gas generally persists at $1\text{--}2$ AU after the dispersal of gas at $10\text{--}100$ AU. The one exception to this is the flattest (R^{-1}) profile, which contains relatively more mass at a large radius. By comparison, some PPDs show large cavities extending out to $\sim 10\text{--}30$ AU (Williams & Cieza 2011), suggesting that – at least in this subset of systems – the raw material for planet formation is concentrated in the outer part of a PPD.

APPENDIX

POST-FU ORI DISK MODEL

Most PPDs may undergo one or many outbursts of accretion in the early stages of their evolution, while the disk is still massive and self-gravity influences its dynamics. These have been named ‘FU Orionis outbursts’ after the first transient of this type to be

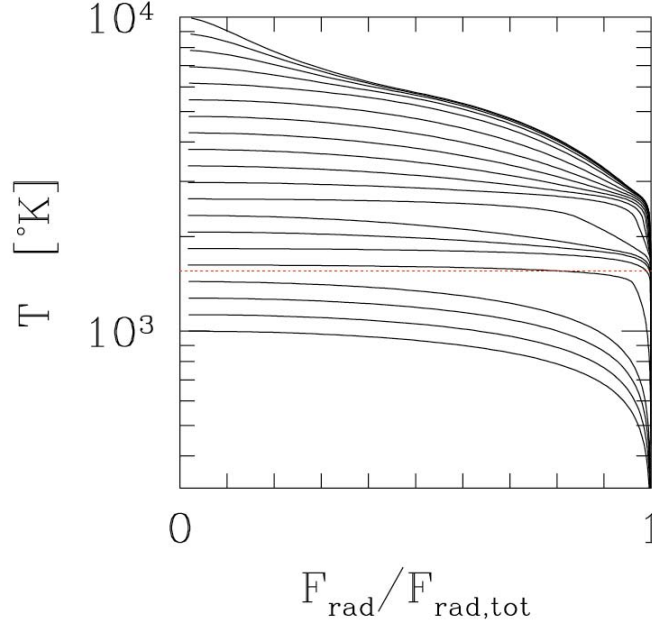


FIG. 17.— Internal temperature of disk constructed from Equations (A1) versus cumulative radiative flux (with $F_{\text{rad}} = 0$ at the disk midplane). Horizontal red dotted line: sublimation temperature of silicate grains. The dissipation in the disk is concentrated almost entirely at $T > T_{\text{sub}}$ or $< T_{\text{sub}}$ except for a narrow range of $T(0)$.

discovered. An interesting feature of theoretical models of such outbursts (e.g. Zhu et al. 2009) is that the surface density profile inside $\sim 1-2$ AU departs significantly from the MMSN model. In fact, the surface density at ~ 0.1 AU can drop well below the corresponding value in the MMSN.

In time-dependent calculations which assume a layered disk with uniform α , Σ_g grows inside ~ 1 AU following an outburst. We show in Section 6 that the opposite behavior is encountered if the seed magnetic field in the inner disk is dominated by the stellar wind immediately following the outburst.

Two significant feedbacks contribute to the growth of the MRI during a FU Ori type outburst. First, the ionization level shoots up deep in the disk (at $\Sigma_g \gtrsim \delta \Sigma_{g,\text{ion}}$) when the temperature is high enough ($T \gtrsim 1500$ K) for silicate dust to sublimate. Then free electrons are no longer absorbed on the surfaces of grains, which are rapidly dispersed throughout the disk column following the catastrophic fragmentation of macroscopic particles high in the disk (Section 5). The second feedback occurs above several 10^3 K as electronic transitions of H and scattering off H^- contribute significantly to the opacity.

Our focus here is on the aftermath of a FU Ori outburst, and so we consider the profile of the disk when it transitions back to a dust-loaded state with strong MRI growth restricted to ionized surface layers (Gammie 1996). To this end, we have constructed uniform- α vertical disk models using the analytic fit to dust, molecular, atomic, free-free and bound-free opacity (collectively denoted by κ) provided by Zhu et al. (2009).

Radiation transfer near the photosphere is handled using the Eddington approximation. The entire disk is assumed to be radiative, and convection is neglected. Hence the equations solved are

$$\begin{aligned}
 \frac{dP}{dz} &= -\Omega^2 z \frac{P \mu_g}{k_B T}; \\
 \frac{dF_{\text{diss}}}{dz} &= \frac{9}{4} \alpha \Omega P; \\
 \frac{dF_{\text{rad}}}{dz} &= \rho \kappa (aT^4 - U_{\text{rad}}) c; \\
 \frac{dU_{\text{rad}}}{dz} &= -3 \frac{\rho \kappa}{c} F_{\text{rad}}; \\
 F_{\text{rad}} &= F_{\text{diss}}.
 \end{aligned} \tag{A1}$$

The lower boundary condition at $z = 0$ is $F_{\text{rad}} = F_{\text{diss}} = 0$, and the upper boundary conditions at large z are $P = 0$; $F_{\text{rad}} = cU_{\text{rad}}/\sqrt{3}$. We do not explore here the origin of the seed field during the outburst, in particular the possibility that it is also derived from the

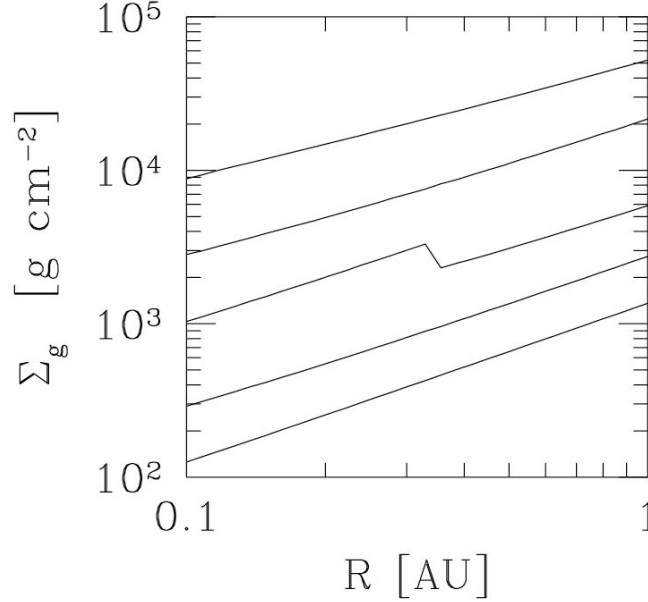


FIG. 18.— Surface density versus radius of a disk with $T(0)$ adjusted to produce one-half of the outgoing radiative flux at $T > T_{\text{sub}}$, and one-half at lower temperatures. Disks with surface density below this critical value are dust loaded; those with higher surface densities are almost entirely dust free. Curves correspond to different values of α , ranging from 0.1 (bottom) to 10^{-5} (top).

stellar wind. Hence α is simply taken to be independent of height.

The solution to Equations (A1) has the property that the upward radiative flux is generated in zones that are entirely above or below the sublimation temperature. Figure 17 shows a sequence of models of increasing midplane temperature $T(0)$; the horizontal red dotted line denotes the sublimation temperature used in the opacity fit. Only for a narrow range of $T(0)$ is there a significant contribution to the outgoing radiative flux from layers with $T < T_{\text{sub}}$ and $T > T_{\text{sub}}$.

We identify the critical $T(0)$ for which one-half of the outgoing radiative flux is generated at $T > T_{\text{sub}}$ (or $< T_{\text{sub}}$), a plot it in Figure 18 as a function of R for various values of α . To initialize our post-FU Ori outburst calculation, we choose the curve corresponding to $\alpha = 10^{-2}$ (Equation (46)). This disk solution implies gravitational instability beyond ~ 2 AU. To avoid that, we smoothly interpolate to a marginally gravitationally unstable disk with $Q = c_g \Omega / \pi \Sigma_g = 2$ beyond ~ 2 AU.

The further evolution of Σ_g in the inner disk is insensitive to the details of this initial profile. The chosen value of Q in the outer disk does influence whether this material can be entirely removed using the prescription of Owen et al. (2012) for a X-ray/FUV-driven wind: that happens for $Q = 20$ but not for $Q = 2$.

REFERENCES

- Bai, X.-N. 2014, *ApJ*, 791, 137
 Bai, X.-N., & Goodman, J. 2009, *ApJ*, 701, 737
 Bai, X.-N., & Stone, J. M. 2011, *ApJ*, 736, 144
 Bai, X.-N., & Stone, J. M. 2013, *ApJ*, 769, 76
 Blaes, O. M., & Balbus, S. A. 1994, *ApJ*, 421, 163
 Calvet, N. 1997, *Herbig-Haro Flows and the Birth of Stars*, 182, 417
 Chambers, J. E., Wetherill, G. W., & Boss, A. P. 1996, *Icarus*, 119, 261
 Chiang, E. I., & Goldreich, P. 1997, *ApJ*, 490, 368
 Chiang, E. I., Joungh, M. K., Creech-Eakman, M. J., et al. 2001, *ApJ*, 547, 1077
 Chiang, E., & Youdin, A. N. 2010, *Annual Review of Earth and Planetary Sciences*, 38, 493
 Chiang, E., & Laughlin, G. 2013, *MNRAS*, 431, 3444
 Chokshi, A., Tielens, A. G. G. M., & Hollenbach, D. 1993, *ApJ*, 407, 806
 Clarke, C. J., Gendrin, A., & Sotomayor, M. 2001, *MNRAS*, 328, 485
 D'Alessio, P., Cantó, J., Calvet, N., & Lizano, S. 1998, *ApJ*, 500, 411
 D'Alessio, P., Calvet, N., Hartmann, L., Lizano, S., & Cantó, J. 1999, *ApJ*, 527, 893
 D'Alessio, P., Calvet, N., Hartmann, L., Franco-Hernández, R., & Servín, H. 2006, *ApJ*, 638, 314
 Duffell, P. C., Haiman, Z., MacFadyen, A. I., D'Orazio, D. J., & Farris, B. D. 2014, *ApJ*, 792, LL10
 Flock, M., Henning, T., & Klahr, H. 2012, *ApJ*, 761, 95
 Fromang, S., & Stone, J. M. 2009, *A&A*, 507, 19
 Funk, B., Wuchterl, G., Schwarz, R., Pilat-Lohinger, E., & Eggl, S. 2010, *A&A*, 516, A82
 Furlan, E., Hartmann, L., Calvet, N., et al. 2006, *ApJS*, 165, 568
 Gammie, C. F. 1996, *ApJ*, 457, 355
 Goldreich, P., & Ward, W. R. 1973, *ApJ*, 183, 1051
 Goldreich, P., & Tremaine, S. 1980, *ApJ*, 241, 425
 Gressel, O., Turner, N. J., Nelson, R. P., & McNally, C. P. 2015, *ApJ*, 801, 84
 Guan, X., & Gammie, C. F. 2009, *ApJ*, 697, 1901
 Hawley, J. F., Gammie, C. F., & Balbus, S. A. 1995, *ApJ*, 440, 742
 Hayashi, C. 1981, *Progress of Theoretical Physics Supplement*, 70, 35
 Hernández, J., Hartmann, L., Megeath, T., et al. 2007, *ApJ*, 662, 1067
 Holsapple, K. A., *Annu. Rev. Earth Planet. Sci.*, 21, 333
 Housen, K. R., Schmidt, R. M., & Holsapple, K. A. 1983, *J. Geophys. Res.*, 88, 2485
 Igea, J., & Glassgold, A. E. 1999, *ApJ*, 518, 848
 Ilgner, M., & Nelson, R. P. 2006, *A&A*, 445, 205
 Jacquet, E., & Balbus, S. 2012, *MNRAS*, 423, 437

- Jacquet, E., & Thompson, C. 2014, *ApJ*, 797, 30
- Klahr, H. H., & Bodenheimer, P. 2003, *ApJ*, 582, 869
- Kretke, K. A., & Lin, D. N. C. 2007, *ApJ*, 664, L55
- Lesur, G., & Longaretti, P.-Y. 2009, *A&A*, 504, 309
- Lesur, G., Kunz, M. W., & Fromang, S. 2014, *A&A*, 566, AA56
- Lissauer, J. J., Dawson, R. I., & Tremaine, S. 2014, *Nature*, 513, 336
- Lubow, S. H., Seibert, M., & Artymowicz, P. 1999, *ApJ*, 526, 1001
- Marcus, P., Pei, S., Jiang, C.-H., et al. 2014, *arXiv:1410.8143*
- Matt, S., & Pudritz, R. E. 2005, *ApJ*, 632, L135
- Menou, K., & Goodman, J. 2004, *ApJ*, 606, 520
- Mohanty, S., Ercolano, B., & Turner, N. J. 2013, *ApJ*, 764, 65
- Newcomb, W. A. 1961, *Physics of Fluids*, 4, 391
- Ogihara, M., Morbidelli, A., & Guillot, T. 2015, *A&A*, 578, A36
- Okuzumi, S., & Hirose, S. 2011, *ApJ*, 742, 65
- Owen, J. E., Clarke, C. J., & Ercolano, B. 2012, *MNRAS*, 422, 1880
- Lynden-Bell, D., & Pringle, J. E. 1974, *MNRAS*, 168, 603
- Paardekooper, S.-J., Baruteau, C., & Kley, W. 2011, *MNRAS*, 410, 293
- Pudritz, R. E., & Norman, C. A. 1986, *ApJ*, 301, 571
- Russo, M., & Thompson, C. 2015, *ApJ*, in press
- Sano, T., & Stone, J. M. 2002, *ApJ*, 577, 534
- Sekiya, M. 1998, *Icarus*, 133, 298
- Simon, J. B., & Hawley, J. F. 2009, *ApJ*, 707, 833
- Smith, A. W., & Lissauer, J. J. 2009, *Icarus*, 201, 381
- Strom, K. M., Strom, S. E., Edwards, S., Cabrit, S., & Skrutskie, M. F. 1989, *AJ*, 97, 1451
- Suzuki, T. K., Muto, T., & Inutsuka, S.-i. 2010, *ApJ*, 718, 1289
- Syer, D., & Clarke, C. J. 1995, *MNRAS*, 277, 758
- Tanaka, H., Takeuchi, T., & Ward, W. R. 2002, *ApJ*, 565, 1257
- Toomre, A. 1964, *ApJ*, 139, 1217
- Turner, N. J., & Sano, T. 2008, *ApJ*, 679, L131
- Ward, W. R. 1991, *Lunar and Planetary Science Conference*, 22, 1463
- Wardle, M., & Salmeron, R. 2012, *MNRAS*, 422, 2737
- Weidenschilling, S. J. 1977, *MNRAS*, 180, 57
- Williams, J. P., & Cieza, L. A. 2011, *ARA&A*, 49, 67
- Winn, J. N., & Fabrycky, D. C. 2015, *Annu. Rev. Astron. Astrophys.*, 53, 409
- Zhu, Z., Hartmann, L., & Gammie, C. 2009, *ApJ*, 694, 1045
- Zsom, A., Ormel, C. W., Güttler, C., Blum, J., & Dullemond, C. P. 2010, *A&A*, 513, A57